The Evolution of an Observed Cold Front. Part I: Numerical Simulation

BRUCE B. ROSS AND ISIDORO ORLANSKI

Geophysical Fluid Dynamics Laboratory/NOAA, Princeton University, Princeton, NJ 08540

(Manuscript received 16 June 1981, in final form 29 October 1981)

ABSTRACT

The 48 h evolution of an observed cold front is simulated by a three-dimensional mesoscale-numerical model for a typical springtime synoptic situation over the southeastern United States. The model used in this study employs anelastic equations of motion on a limited-area domain with locally determined inflow/outflow side boundaries.

Both the observed and simulated characteristics of the weather system indicate a mature front which intensifies and then weakens over the 48 h period. Moist convection occurs in the form of intermittent squall lines in the observed case; in the numerical simulation, convection develops above and somewhat ahead of the surface front after 24 h as an ensemble of convective cells.

An investigation is made of the mesoscale and subsynoptic-scale features of this solution to determine their sensitivity to the inclusion of moisture and to the magnitude of the eddy viscosity used in the numerical simulation. The primary effect of increased eddy viscosity is to reduce somewhat the propagation speed of the front. The major changes due to moisture inclusion occur when convection develops along the cold front; these convective effects, which are apparent in the subsynoptic as well as the mesoscale features of the solution, include increased low-level convergence, reduced surface pressure due to diabatic heating, and the deflection of winds due to upper-level divergence. In addition, small temperature changes occur in the middle troposphere between the jet stream and the surface front when either viscosity or moisture is varied; these disturbances are a clear manifestation of the effect which changes in the cross-stream circulation intensity have upon the frontal system.

A fundamental feature of the mesoscale structure of the front in all cases is the tendency of the line of maximum horizontal convergence at the surface to move ahead of the line of maximum vertical vorticity. This phase shift appears to be related to the propagation characteristics of the frontal system. Also, the mesoscale moist convection develops a cellular structure throughout the convective zone in the low-viscosity solution; the use of higher viscosity tends to suppress these cells, particularly near the surface.

1. Introduction

Since the early 1970's, major advances have been made in our understanding of frontogenetic processes in baroclinic waves, largely through the work of Hoskins (1971), Williams (1967), and others. At the same time, however, only limited progress has been achieved in describing the dynamic balances which characterize mature fronts. The fundamental question to be considered regarding the dynamics of such fronts is, what changes in the developing cold front inhibit further frontogenesis and produce a balanced, steady-state condition?

Simplified dynamic models with idealized initial conditions indicate that dissipation and surface friction are required to offset frontogenetic terms such as the vertical stretching of vorticity near the surface and thereby to produce a balanced state. In particular, Hoskins and West (1979) rely upon dissipative effects to limit frontal development in their three-dimensional simulations of cold and warm fronts using a semi-geostrophic system of equations. As the work of McWilliams and Gent (1980) and Blumen (1980) suggests, these semi-geostrophic equations may fail to simulate certain ageostrophic effects in the frontal dynamics. These effects may be as important as dissipation in balancing frontogenetic processes during the later stages of cold-frontal development. For example, Orlanski and Ross (1977) have shown in a two-dimensional numerical solution that the cross-stream circulation within the frontal system may also retard further frontal intensification when this circulation reaches a finite amplitude. It therefore seems appropriate to use a primitive-equation, three-dimensional numerical model to simulate an observed cold front case in order to determine whether other ageostrophic mechanisms besides dissipation act to balance frontogenetic effects.

Proper representation of the ageostrophic circulation is important not only because of its significance to the dynamic balance of the mature front but also because of its relevance to the development of prefrontal moist convection (Ross and Orlanski, 1978, referred to hereafter as RO). In particular, this circulation may imply when and where frontal rainbands occur within the frontal system. Recent

observations of mesoscale convection, particularly of rainbands and squall lines (Zipser, 1977; Hobbs and Biswas, 1979; James and Browning, 1979; Ogura and Liou, 1980), have revealed many interesting features, including the spatial distribution of convective cells within rainbands and the role of mid-tropospheric convergence in the maintenance of deep convection. Numerical simulations with sufficient spatial resolution may provide us with the means to improve our understanding of both the associated synoptic-scale processes and the mesoscale convection itself.

In this article and a companion paper, we will attempt to simulate an observed case of frontal evolution and squall-line development. Our goal in this effort is to better understand the role which ageostrophic, subsynoptic effects play in maintaining the frontal cross-stream circulation and to determine the influence which this cross-stream circulation has in initiating and sustaining a line of deep convection. Furthermore, the structure of this convection will be analyzed in detail and will be compared to the observed structure of other extratropical squall-lines.

In the present paper, the open-boundary, three-dimensional numerical model is described in detail (Section 2). Then the synoptic situation to be simulated is described, and a comparison is made between observations and the numerical simulation (Section 3). Finally, an analysis is presented of the sensitivity of the simulation to the presence of moisture and to the magnitude of the parameterized eddy viscosity (Sections 4 and 5). In this analysis, a distinction is made between the effects of these parameters on subsynoptic or meso-α features and on mesoscale or meso-β features.

The second paper (Orlanski and Ross, 1982) will present a more detailed analysis of the vorticity and divergence fields in both the dry and moist frontal cases. Also, the development and structure of the convection within the frontal system will be investigated in more detail, and the different transport terms within the convective zone will be compared to each other.

Readers who are not interested in the details of the numerical model may proceed immediately to Section 3.

2. The numerical model

The three-dimensional numerical model used in this study employs a finite-difference representation of the equations of motion, as defined on a limited-area domain. Major features of interest in the model are: (a) open boundary conditions which determine momentum and thermodynamic variables according to local inflow/outflow conditions, (b) explicit representation of moist convection so as to better portray the interaction of convection with large-scale dynamics, (c) the use of the anelastic formulation of Ogura and Phillips (1962) for the equations of motion in order to permit both hydrostatic and non-hydrostatic solutions, and (d) the capability to run the model in a one-way nesting mode. The model uses a stereographic projection to map the limited area domain onto a Cartesian grid with physical height z as the vertical coordinate. The vertical coordinate grid spacing is determined by a prescribed mapping function $G(\sigma)$ according to the approach of Orlanski *et al.* (1974). Neither map factors nor topography are included in this initial version of the model.

Initial conditions and time-dependent boundary data for a given model run are obtained either from observational data or from a coarser nested solution. A hierarchy of models may be defined with different horizontal spatial resolutions which are progressively finer. In the present case, we employ a sequence of runs in which the coarser model with 246-km grid size [to match the local "N40 grid" of Miyakoda (1973)] uses observations to determine boundary and initial data. This model then generates a data set which is used to prescribe boundary and initial data for the finer model with a 61.5-km grid size. The equations and boundary condition treatment are the same in the fine and coarse models. The parameters used in each model are identical with the exception of those which depend upon grid size or geography (e.g., surface-boundary conditions which reflect land–sea differences).

a. Basic equations

The anelastic equations describe perturbations of the atmosphere from an isentropic base state at rest, as postulated by Ogura and Phillips (1962). The base state is defined by a uniform potential temperature θ_0 with the reference density ρ_0 and the Exner pressure π_0 (defined as $(P_0/P_{\text{surf}})^{R/c_p}$ with $P_{\text{surf}} = 1000$ mb) only dependent upon the vertical coordinate, z.

The equation for horizontal momentum is given in vector form as

$$\frac{\partial}{\partial t}(\rho_0 \mathbf{V}) = -\nabla\cdot(\rho_0 \mathbf{V}\mathbf{V}) - G\frac{\partial}{\partial \sigma}(\rho_0 w \mathbf{V}) - c_p\theta_0\nabla(\rho_0\pi) - f\mathbf{k}\times\rho_0\mathbf{V} + \nabla\cdot\tau + G\frac{\partial}{\partial\sigma}\mathbf{k}\cdot\tau, \tag{2.1}$$

where the vector $\mathbf{V}$ is the horizontal wind velocity with components u and v in the x- and y-directions respectively and w is the wind component in the z-direction, that is, in the direction of the unit vector $\mathbf{k}$. The operator ∇ will be assumed to be horizontal, i.e.,

$$\nabla \equiv \frac{\partial}{\partial x}\mathbf{i} + \frac{\partial}{\partial y}\mathbf{j}.$$

The vertical component of the Coriolis parameter, f, varies in x and y. The vertical stretching coordi-

nate, σ, is related to the physical coordinate z by the transformation $G(\sigma) = d\sigma/dz$ where G in the present case will be equal to the constant $1/H$ with H the height of the rigid lid.[1] The last two terms of (2.1) represent the divergence of the stress tensor τ which is expressed in subscript notation as

$$\tau_{pq} = \rho_0 \nu^P \left(\frac{\partial u_q}{\partial x_p} + \frac{\partial u_p}{\partial x_q} - \delta_{pq} \frac{2}{3} \frac{\partial u_r}{\partial x_r} \right), \qquad (2.2)$$

where $\partial u_r/\partial x_r$ is equivalent to $\sum_{r=1}^{3} (\partial u_r/\partial x_r)$, δ_{pq} is the Kronecker delta, and ν^P denotes the eddy viscosity components which will be discussed later. Note that expression (2.2) reduces to the Navier-Stokes stress tensor if ν^P becomes the molecular viscosity. The parameterization of subgrid turbulence does not require τ to be in this form. This form was chosen because the model does not contain any fundamental assumptions which preclude its use for basic laboratory-scale fluid experiments; the form of (2.2) therefore permits the viscosity formulation to be extended to the molecular limit in order to model small-scale hydrodynamic flows.

The form of the continuity equation under the anelastic approximation is

$$G \frac{\partial}{\partial \sigma} (\rho_0 w) = -\nabla \cdot (\rho_0 \mathbf{V}), \qquad (2.3)$$

which provides a diagnostic equation for w in the hydrostatic case treated here.

The prognostic equations for the thermodynamic variables θ, q, and c are given as

$$\frac{\partial \theta}{\partial t} = -\mathbf{V} \cdot \nabla \theta - wG \frac{\partial \theta}{\partial \sigma} + \frac{L}{c_p \pi_0} \left(\frac{\partial c}{\partial t} \right)_{\text{cond}} - \frac{1}{\rho_0} \nabla \cdot \mathbf{F}^\theta - \frac{1}{\rho_0} G \frac{\partial}{\partial \sigma} (\mathbf{k} \cdot \mathbf{F}^\theta), \qquad (2.4)$$

$$\frac{\partial q}{\partial t} = -\mathbf{V} \cdot \nabla q - wG \frac{\partial q}{\partial \sigma} - \left(\frac{\partial c}{\partial t} \right)_{\text{cond}} - \frac{1}{\rho_0} \nabla \cdot \mathbf{F}^q - \frac{1}{\rho_0} G \frac{\partial}{\partial \sigma} (\mathbf{k} \cdot \mathbf{F}^q), \qquad (2.5)$$

and

$$\frac{\partial c}{\partial t} = -\mathbf{V} \cdot \nabla c - wG \frac{\partial c}{\partial \sigma} + \left(\frac{\partial c}{\partial t} \right)_{\text{cond}} - \frac{1}{\rho_0} \nabla \cdot \mathbf{F}^c - \frac{1}{\rho_0} G \frac{\partial}{\partial \sigma} (\mathbf{k} \cdot \mathbf{F}^c), \qquad (2.6)$$

where q and c are mixing ratios of water vapor and cloud water respectively. The eddy fluxes are of the form

$$\mathbf{F}^\phi = -\rho_0 \kappa^H \nabla \phi - \rho_0 \kappa^v G \frac{\partial \phi}{\partial \sigma} \mathbf{k}, \qquad (2.7)$$

where ϕ denotes θ, q, or c, and κ^H and κ^v are respectively the horizontal and vertical eddy diffusivities.

The effects of water phase changes are denoted schematically by the quantity $\left(\frac{\partial c}{\partial t} \right)_{\text{cond}}$ in (2.4)–(2.6). The phase change amount for each time step is determined by a modified and more accurate version of the moisture adjustment procedure described by RO.

In this method, the values of $q^{\tau+1}$ and $c^{\tau+1}$ which are predicted for time $(\tau + 1)\Delta t$ using advection and diffusion alone are altered so that the water vapor mixing ratio does not exceed $Kq_s^{\tau+1}$. The factor K, assumed here to be 0.95, is the effective relative humidity at which condensation is assumed to occur within each grid box (Smagorinsky, 1960; RO). The saturation mixing ratio $q_s^{\tau+1}$ depends upon potential temperature $\theta^{\tau+1}$ as

$$q_s^{\tau+1} = \tilde{q}_s \exp\left[\frac{L\tilde{\pi}}{R_v \tilde{T}^2} (\theta^{\tau+1} - \tilde{\theta}) \right], \qquad (2.8)$$

where L is the heat of condensation, R_v is the gas constant for water vapor, and quantities with tildes refer to the reference base state obtained by averaging the model initial condition fields in the horizontal.[2]

However, because $(\partial c/\partial t)_{\text{cond}}$ depends upon $\theta^{\tau+1}$ through (2.8), Eq. (2.4) becomes a nonlinear equation in $\theta^{\tau+1}$. Ross and Orlanski solved this equation by expressing (2.8) with a centered time derivative. The drawback of this approach is that the prognostically predicted $q_s^{\tau+1}$ differs from the value determined by (2.8) for $\theta^{\tau+1}$ because of time truncation errors. In the present technique, we avoid this disparity by computing $\theta^{\tau+1}$ from the full nonlinear equation using Newton-Raphson methods.

Finally, the perturbation Exner pressure π which appears in the momentum equation (2.1) is computed from the hydrostatic equation

$$c_p \theta_0 \frac{\partial \pi}{\partial z} = g \left(\frac{\theta}{\theta_0} + 0.608q - c \right). \qquad (2.9)$$

In Section 2c, we will present the methods used to compute the pressure at the rigid model lid, which is needed along with this equation to determine the complete pressure field.

[1] Because vertical stretching of z is not employed in the present case, we use z rather than σ as the vertical coordinate in expressions to be presented in the model description which follows.

[2] This base state is believed to give more accurate moisture results than the isentropic base state used by Ross and Orlanski.

b. Eddy parameterization

Our intention here is to employ a single parameterization of subgrid-scale turbulence for the entire range of phenomena to be simulated by the various nested models. The primary quantity used to determine the eddy viscosity and diffusivity is the local Richardson number Ri, defined as

$$\mathrm{Ri} = \frac{g}{\theta_0} \frac{\theta_z}{(u_z^2 + v_z^2)}.$$

In theoretical studies whenever a local value of Ri is defined, the physical length scale which is appropriate for the fluid-dynamical phenomenon of interest is used. In a numerical model, on the other hand, the local Richardson number is limited by the grid size of the model, which may be much larger than the scale of the turbulence which is to be parameterized. Thus, the value of Ri will serve as a bulk Richardson number which indicates the sensitivity of the mean flow to an integrated effect of the turbulence to be parameterized. This bulk Richardson number must have the same limiting characteristics as the local value of Ri, namely, that the flow be very stable with low eddy viscosity when bulk $\mathrm{Ri} \gg 0$ and that it be very unstable with high eddy viscosity when bulk $\mathrm{Ri} \leq 0$. The obvious difficulty comes in choosing the critical Richardson number, Ri_c, below which the atmosphere becomes turbulent. In the laboratory, the value of Ri_c is found to be around 0.25, but the value for bulk Richardson number in an atmospheric numerical model is closer to unity, reflecting the fact that it represents the average conditions over some vertical layer which may contain both stable and unstable regions. Then if one chooses the values of maximum and minimum eddy viscosity expected to occur in a grid box of the model for extreme conditions (negative and large positive Ri respectively), a straight-forward approach would be to represent the eddy viscosity as a hyperbolic tangent function of Ri centered at the critical Richardson number Ri_c. This approach has the advantage that a range Δ Ri can be prescribed which defines the transition interval from low to high turbulent intensity. This gives less importance to the choice of Ri_c, which will be somewhat arbitrary. Accordingly, the expression for the vertical viscosity ν^v is

$$\nu^v = \nu_0^v + (\nu_f^v - \nu_0^v)\left[1 - \tanh\left(\frac{\mathrm{Ri} - \mathrm{Ri}_c}{\Delta\,\mathrm{Ri}}\right)\right].$$

In practice, it is more convenient to use an exponential form of this expression, namely:

$$\nu^v = \exp\left[A \tanh\left(\frac{\mathrm{Ri} - \mathrm{Ri}_c}{\Delta\,\mathrm{Ri}}\right) + B\right] \ln 10, \quad (2.10)$$

where A and B are determined such that

$$\nu^v \to \nu_0^v \quad \text{as} \quad \mathrm{Ri} \to \infty$$

and

$$\nu^v \to \nu_f^v \quad \text{as} \quad \mathrm{Ri} \to -\infty.$$

A turbulent Prandtl number of unity is assumed so that $\kappa^v = \nu^v$. The horizontal values ν^H and κ^H are equal to the local values of ν^v and κ^v increased by a constant factor which is assumed to be roughly proportional to $(\Delta x/\Delta z)^2$.

In the moist atmosphere which we will be treating, the appropriate variable to indicate instability should be equivalent potential temperature θ_e rather than θ alone in the expression for Ri. In the present study, however, we have chosen instead to produce the effect of moist convection upon the eddy viscosity by increasing the value of the critical Richardson number in regions of the domain which are presumed to be more turbulent.

As a first attempt at this, the value of Ri_c was increased from its normal value of one in unsaturated air to a value of 100 where saturation occurred ($q > 0.95q_s$). This procedure, which effectively increased ν^v to ν_f^v in cloud areas, was obviously effective in controlling moist convection intensity in the model. Nevertheless, it had several drawbacks. First of all, it made cloud zones very viscous, an effect which was especially unfortunate when the moist air was convectively stable and would not produce intense turbulence in the real atmosphere. Also, when active convection occurred, downdraft regions in the vicinity of the convection would be too inviscid where the air was unsaturated and stable but the vertical motion was intense.

An alternate approach to the above procedure and the approach used in the present study utilizes vertical motion as the indicator of turbulent intensity for the critical Richardson number through the expression

$$\mathrm{Ri}_c = \left(1 + \frac{|w|}{w^*}\right)\mathrm{Ri}_{c_0},$$

where the parameter w^* is the critical vertical velocity, which should be dependent upon the horizontal resolution of the numerical model, and Ri_{c_0} is the basic critical Richardson number, which will be assumed to be equal to 1. This approach has been shown to be quite successful in the model because it not only parameterizes turbulence in areas of deep convection[3] but also gives a reasonable nonlinear

[3] As noted earlier in this section, the horizontal viscosity ν^H is proportional to the vertical viscosity ν^v according to the ratio of the squares of the horizontal to vertical grid sizes. If convection were explicitly resolved without the need for an eddy parameterization, the horizontal and vertical heat fluxes would be similar in magnitude. Therefore, when an eddy parameterization is used, the ratio of the horizontal to vertical eddy viscosity coefficients should be proportional to the square of the ratio $\Delta x/\Delta z$ to achieve the same effect. Results also indicate that this eddy parameterization effectively controls the tendency of convection in a hydrostatic system to excite the smallest resolvable scales.

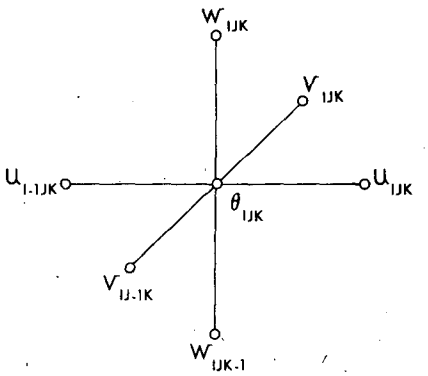

FIG. 1. Schematic diagram showing staggered grid used in the model.

dissipation for stratospheric internal gravity waves which otherwise would remain undamped because of the very stable lapse rate. A value of 2.5 cm s^{-1} is used for w^* in the 61.5 km grid solutions presented in this paper.

c. Numerical formulation

Eqs. (2.1)–(2.7) are expressed in a finite-difference form similar to that used by Williams (1969) and others. The momentum variables, $\rho_0 u$, $\rho_0 v$, and $\rho_0 w$, are staggered in a three-dimensional lattice about the potential temperature point, which is the spatial location of all the thermodynamic and moisture variables as well. This grid staggering (see Fig. 1), which corresponds to the "C Grid" in Arakawa's terminology (Meisinger and Arakawa, 1976), is useful in minimizing the truncation errors for the continuity equation (2.3), although it produces higher truncation error in the Coriolis terms of the momentum equations (2.1). Since the primary use for this model is for scales of meso-α size or smaller, we believe that greater accuracy is required for the continuity equation, which would affect gravity waves and convective phenomena, than is needed for the larger-scale Coriolis effects.

Because of the rigid lid which is assumed for the top boundary of the model (see Section 2d for a more detailed description of boundary conditions), it is convenient to separate the horizontal wind field in the model into barotropic and baroclinic parts. This follows because the upper boundary condition that $w = 0$ at $z = H$ implies that the integral of the horizontal divergence over the depth of the air column should vanish, i.e.,

$$\int_0^H \nabla \cdot \rho_0 \mathbf{V} dz = 0,$$

or simply that

$$\nabla \cdot \overline{\rho_0 \mathbf{V}} = 0, \tag{2.11}$$

if the barotropic momentum $\overline{\rho_0 \mathbf{V}}$ is defined as

$$\overline{\rho_0 \mathbf{V}} \equiv \frac{1}{H} \int_0^H \rho_0 \mathbf{V} dz, \tag{2.12a}$$

while the baroclinic momentum $(\rho_0 \mathbf{V})'$ is defined as

$$(\rho_0 \mathbf{V})' \equiv \rho_0 \mathbf{V} - \overline{\rho_0 \mathbf{V}}. \tag{2.12b}$$

[Note that these definitions include density ρ_0 because of the anelastic deep convection form of the continuity equation, (2.3)]. Since (2.11) applies only to the barotropic part of the momentum, it is useful to deal with the barotropic and baroclinic parts separately; thus, the finite difference form of the momentum equation (2.1) will be separated into the barotropic equation

$$\overline{\rho_0 \mathbf{V}}^{\tau+1} = \overline{\rho_0 \mathbf{V}}^{\tau-1} + 2\Delta t\{\bar{\mathbf{G}} - c_p \theta_0 \nabla \overline{\rho_0 \pi}\} \tag{2.13}$$

and the baroclinic equation

$$(\rho_0 \mathbf{V}^{\tau+1})' = (\rho_0 \mathbf{V}^{\tau-1})' - 2\Delta t\{\mathbf{G}' + c_p \theta_0 \nabla(\rho_0 \pi)'\}, \tag{2.14}$$

where the time derivative has been written in the "leapfrog" finite-difference form used in the model. Superscripts "$\tau + 1$" and "$\tau - 1$" refer to times $(\tau + 1)\Delta t$ and $(\tau - 1)\Delta t$ respectively in the normal way (superscripts have been dropped from variables for the time $\tau \Delta t$). The vector $\mathbf{G}$ represents the terms for advection, Coriolis force, and stress. Bar and prime quantities use the definitions of (2.12).

Eqs. (2.13) and (2.14) represent prognostic equations for $\overline{\rho_0 \mathbf{V}}^{\tau+1}$ and $(\rho_0 \mathbf{V}^{\tau+1})'$ in which all of the quantities on the right-hand side are known except for the Exner pressure. This pressure is determined as

$$\pi = \pi_{\text{lid}} + \pi_H, \tag{2.15}$$

where π_{lid} is the pressure on the rigid lid at height $z = H$ and π_H is the hydrostatic pressure calculated from (2.9) as the integral

$$\pi_H = -\frac{g}{c_p \theta_0} \int_z^H \left(\frac{\theta}{\theta_0} + 0.608q - c\right) dz. \tag{2.16}$$

The pressure π_{lid} may be viewed as that pressure needed on the lid of the model so that the vertical velocity of the fluid at $z = H$ remains zero. In order to derive an expression for the quantity π_{lid}, we multiply (2.15) by ρ_0 and take the barotropic part so that

$$\overline{\rho_0 \pi} = \bar{\rho}_0 \pi_{\text{lid}} + \overline{\rho_0 \pi_H}.$$

Then, solving for π_{lid}, we obtain

$$\pi_{\text{lid}} = \frac{\overline{\rho_0 \pi} - \overline{\rho_0 \pi_H}}{\bar{\rho}_0}, \tag{2.17}$$

where we now must determine the variations of $\overline{\rho_0 \pi}$ in x and y such that the barotropic momentum

field $\overline{\rho_0 \mathbf{V}}$ remains non-divergent as required by (2.11). If we take the divergence of (2.13), then the condition that the barotropic divergence be steady is sufficient to produce the required two-dimensional Poisson equation for $\overline{\rho_0 \pi}$:

$$\nabla^2 \overline{\rho_0 \pi} = \frac{\nabla \cdot \bar{\mathbf{G}}}{c_p \theta_0}. \tag{2.18}$$

Boundary conditions for this elliptic equation will be discussed in Section 2d.

The solution $\overline{\rho_0 \pi}$ from (2.18) then provides the needed information to solve for π using Eqs. (2.15)–(2.17).[4] The prognostic momentum equations (2.13)–(2.14) may then be solved for $\overline{\rho_0 \mathbf{V}}^{\tau+1}$ and $(\rho_0 \mathbf{V}^{\tau+1})'$. In the present version of the model, however, we will employ a different method from the direct use of (2.13) to obtain $\overline{\rho_0 \mathbf{V}}^{\tau+1}$. In particular, rather than trying to maintain the zero barotropic divergence of the initial fields through use of (2.13) and (2.18), we will require nondivergence in $\overline{\rho_0 \mathbf{V}}$ by defining it in terms of a streamfunction ψ such that

$$\overline{\rho_0 u}^{\tau+1} = \frac{\partial \psi^{\tau+1}}{\partial y}, \quad \overline{\rho_0 v}^{\tau+1} = -\frac{\partial \psi^{\tau+1}}{\partial x}. \tag{2.19}$$

Taking the curl of (2.13) then gives a prognostic equation for the barotropic vorticity

$$\overline{\rho_0 \zeta}^{\tau+1} = \overline{\rho_0 \zeta}^{\tau-1} + 2\Delta t |\nabla \times \bar{\mathbf{G}}|. \tag{2.20}$$

We may then determine $\psi^{\tau+1}$ by solving the two-dimensional Poisson equation

$$\nabla^2 \psi^{\tau+1} = -\overline{\rho_0 \zeta}^{\tau+1}, \tag{2.21}$$

using the observed (or coarse model) non-divergent boundary velocities normal to the boundaries together with boundary vorticity values described in Section 2d.

Finally we may summarize the equations used by the model to advance the solution from time $\tau \Delta t$ to time $(\tau + 1)\Delta t$. The procedures described are constrained by the practical requirement that only four consecutive x–z slabs from the full three-dimensional arrays be present in the computer primary storage (central memory) when the three-dimensional equations are being evaluated (steps 1 and 3 below). The computational procedure is carried out as follows:

1) Knowing all variables at times $\tau \Delta t$ and $(\tau - 1)\Delta t$, one computes $(\rho_0 \mathbf{V}^{\tau+1})'$, $\theta^{\tau+1}$, $q^{\tau+1}$, and $c^{\tau+1}$ using (2.14), (2.4), (2.5), and (2.6) respectively. The continuity equation (2.3) is used to determine $(\rho_0 w)^{\tau+1}$ from $(\rho_0 \mathbf{V}^{\tau+1})'$.

2) The barotropic quantities $\psi^{\tau+1}$ and $\overline{\rho_0 \pi}^{\tau}$ are determined by solving the two-dimensional Poisson equations, (2.21) and (2.18), respectively.

3) The barotropic momentum implied by $\psi^{\tau+1}$ in step 2 is added to $(\rho_0 \mathbf{V}^{\tau+1})'$ from step 1 to produce the complete momentum $\rho_0 \mathbf{V}^{\tau+1}$. Also, $\overline{\rho_0 \pi}^{\tau}$ from step 2 is used along with the hydrostatic pressure $\pi_H{}^{\tau+1}$ as implied by $\theta^{\tau+1}$, $q^{\tau+1}$, and $c^{\tau+1}$ (2.16) to give the lid pressure $\pi_{\text{lid}}{}^{\tau+1}$ (2.17) and thereby the complete Exner pressure $\pi^{\tau+1}$.

In the solutions presented here, a time step Δt of 180 s was used. A weak time filter (Robert, 1966) was applied in step 3 to suppress the splitting of modes which is associated with the leapfrog time-difference method being employed.

d. Boundary conditions

1) SIDE BOUNDARIES

One of the most critical aspects of any limited-area model is the boundary conditions used to determine variables on the "open" side boundaries of the model. The basic procedure used here, which is described in more detail in Appendix A, is: (1) to use "radiative" (extrapolated) conditions where outflow occurs and (2) to prescribe boundary data from observations or from a coarser model where inflow occurs. Our current approach reflects the same philosophy as that of Orlanski (1976) in that inflow/outflow conditions are determined at each boundary point from local conditions. On the other hand, we now employ only the local advection speed normal to the boundary (specifically, an average between the local interior value and the value from observed or coarse model data) as a determinant of the propagation or phase speed rather than the more sophisticated quantity which was proposed by Orlanski. Our choice of this advection speed alone was motivated primarily by its simplicity of application; moreover, the effects of the propagation of faster gravity-wave modes, which are neglected by this approach, will normally be of only secondary importance for the model resolution used in this case.

The unique feature of the boundary procedure used here is that the higher-order quantities of vertical vorticity ζ and horizontal divergence D are used to determine the wind components u and v at the boundaries. This approach, which is also utilized in the model initialization (Section 2e), reduces distortions at the boundary because derivatives of u and v, rather than u and v themselves, are extrapolated or prescribed at the boundary points.

Although it provides a more accurate representation of flow conditions at the boundary, the localized determination of inflow/outflow has the drawback that it tends to produce large wind shears at those singular points where flow conditions change

[4] In fact, because of practical constraints imposed by programming procedures, $\overline{\rho \pi}^{\tau-1}$ will be used to determine π_{lid} at time $\tau \Delta t$. This approximation produces no significant inaccuracy since π_{lid} varies slowly in time and the time step Δt is only 180 s.

from inflow to outflow. To eliminate this effect without resorting to a layer of large viscosity along the boundary, we apply a one-dimensional Shapiro (1970) smoothing operator to the closed loops of u, v, and θ, which make up the boundary points for the limited-area model. This operator, which is best suited to the periodic functions associated with these boundary loops, has been shown in the 61.5 km grid solution to eliminate waves of wavelength less than $3\Delta x$ along the boundaries, while leaving wavelengths greater than $7\Delta x$ unaltered.

Finally, as described in Section 2c, the rigid-lid condition in the model implies that the wind components u and v should be separated into baroclinic and barotropic parts. The effect of this upon the calculation procedure is that the baroclinic momentum components $(\rho_0 u^{\tau+1})'$ and $(\rho_0 v^{\tau+1})'$ are determined by the prognostic equation (2.14), and the barotropic momentum components $\overline{\rho_0 u}^{\tau+1}$ and $\overline{\rho_0 v}^{\tau+1}$ are found by solving the Poisson equation (2.21) for the streamfunction $\psi^{\tau+1}$. The barotropic boundary velocity components are found by the above open boundary procedure. The observed (or coarse model) barotropic momentum normal to the boundary is used to determine the Dirichlet boundary condition $\psi^{\tau+1}$ for (2.21). Because of the staggered grid used in the model, however, the expression (2.20) is unable to determine the barotropic vorticity $\overline{\rho_0 \zeta}^{\tau+1}$ for the outermost interior points in the forcing function of the Poisson equation. But these outer vorticity points are actually the boundary vorticity values which have been determined by the inflow/outflow procedure described above and in Appendix A. Therefore the barotropic part of this boundary value is used to complete the forcing function $\overline{\rho_0 \zeta}^{\tau+1}$ for (2.21).

2) Surface boundary

Since the present version of the model does not use stretching of the vertical grid, no detailed boundary-layer treatment of the surface boundary conditions is used here.[5] In particular, the surface boundary conditions for θ and q are posed in a simple heuristic way with no attempt made at this time to develop a surface heat and moisture budget procedure. Specifically, the surface condition for potential temperature only requires a constant lapse rate at the surface of 4°C $(1000\ \text{m})^{-1}$, with no diurnal effects included in the present model. The condition for mixing ratio q for solutions involving moisture fixes the relative humidity at the surface at a prescribed value which depends upon whether the point is located over land or ocean. In the solution presented here, the surface relative humidity is fixed at 60% over land and 85% over water with a smoothly varying transition zone of $5\Delta x$ width at the land/sea interface. This moisture boundary condition is included in the model as a way to approximately simulate the important effect of moist air over the Gulf of Mexico as a primary source of moisture for convective activity over the southeastern United States.

Regarding the surface boundary conditions for the wind components, a bulk drag formulation may be used in the model to determine the vertical shear of horizontal wind components at the surface using different drag coefficients over land and ocean. A free slip condition is used, however, in the current solutions. The vertical wind component w is set to zero at the surface with the lower boundary assumed to be flat.

3) Top boundary

Since the upper boundary of the model is located at a height H of 16 km, which is well above most mesoscale activity in the solution, the main purpose of boundary conditions at this level is to provide a means to bound the vertical extent of the model without reflecting gravity waves back to the lower levels to any great extent. To accomplish this, observed (or coarser model) data are used as boundary conditions for $\rho_0 u$, $\rho_0 v$, and θ at the upper boundary. These data are obtained, as are the side boundary values, from a linear time interpolation between observed data at specific time intervals (Section 2e). As a mechanism for reducing wave reflection, Newtonian damping is applied to these three fields at the first level ($z = H - \Delta z$) below the lid using a damping time constant of 2 h so as to drive these variables towards their observed values.

As discussed in Section 2c, the vertical momentum, $\rho_0 w$, is zero at the upper boundary because this boundary is assumed to be rigid. Finally, zero-flux boundary conditions, namely

$$\left.\frac{\partial q}{\partial z}\right|_H = \left.\frac{\partial c}{\partial z}\right|_H = 0,$$

are assumed for the moisture variables.

e. *Initialization*

The techniques used to provide initial and boundary data for the nested models have been developed in order to produce fields which are consistent with the anelastic hydrostatic model and which are interpolated to the finer grid in such a way as to minimize

[5] In the low viscosity cases ML and DL presented below, the background viscosity κ_0^v is increased from the free-atmosphere value of 5 $m^2\ s^{-1}$ to a surface value of 20 $m^2\ s^{-1}$ in the surface layer, $z < 2$ km. This serves to crudely represent the increased viscosity in the planetary boundary layer.

the effects of the coarseness of the coarser grid. No major effort was made to balance the observed data for use in the coarsest model (with $\Delta x = 246$ km)[6] because the rotational part of the wind was already balanced on the hemispheric N40 grid using the streamfunction Poisson equation described by Miyakoda (1973). Also, since the present model uses open boundaries, we believe that any imbalances in the initial fields will be adjusted dynamically with the resulting disturbances propagating out of the domain as gravity waves through the open boundaries.

In the discussion which follows, we will make no distinction between the preparation of initial and boundary data since the procedures used to prepare both data-sets are identical. In the procedure, a complete set of variables is obtained on the chosen model grid at prescribed evenly-spaced times throughout the time period to be modeled. Data at any one of these times may then be used either to initialize the model or to provide boundary data for a model run which was started at an earlier time.

Two different initialization procedures will be described although many of the techniques used in each are identical. In the first method, which we refer to as the coarse-model initialization, data in the N40 format (designated here as "observed") is converted to a form which is appropriate for the coarsest grid in the nested model hierarchy. In the second method, which is called the nested-model initialization, the data from a coarser resolution solution in the nesting hierarchy is mapped to the finer grid, for example from the 246-km grid to the 61.5-km grid in the present case. As one might expect, the initialization from observed data will be more elaborate since it involves the conversion of different types of variables, as well as horizontal and vertical interpolation, while initialization for the nested model primarily consists of horizontal interpolation alone.

One feature common to both initialization procedures is the approach that, wherever possible, interpolation from coarse to fine grids is performed on higher-order quantities such as vorticity and divergence rather than on the basic variables such as u and v. The original u and v may then be reconstructed on the finer grid by solving Poisson equations to obtain streamfunction ψ and velocity potential Φ, both of which then determine the fine-grid flow. This technique, the details of which will be described in a later paper, has the effect of reducing the effects of the interpolation procedure on the raw variables u and v. Note that u and v will have to be interpolated to the fine grid in order to provide boundary conditions for the Poisson equation. Any roughness in the resulting ψ and Φ fields is minimized for the final fine-grid variables by solving the appropriate Poisson equations on grid domains larger than the domain which will ultimately be used by the finer mesoscale model.

The coarse-model initialization procedure uses gridded data which were initialized for the GFDL N40 model and which were originally taken from NMC data sets for 0000 and 1200 GMT of each day. The data consists of stream function ψ, temperature T, geopotential height ϕ, and relative humidity R for 13 standard-pressure levels ranging from 30 mb to 1150 mb. The coarse mesoscale model uses the same grid spacing and orientation as the stereographic N40 grid, although variables in the mesoscale model are staggered in a C-grid configuration rather than the A-Grid form used in the N40 data; therefore the horizontal interpolation required is minimal for this case. On the other hand, the observed variables must be interpolated from constant-pressure to constant-height levels in the vertical using the geopotential heights. After interpolation, the pressure is made compatible with the potential temperature. Finally, the barotropic wind field is put in geostrophic balance with the barotropic pressure field as a balancing procedure. (This balancing procedure has been found in more recent model runs to be unnecessary).

The nested-model initialization is basically an interpolation procedure since the data types of the coarser and finer models are identical. In the present case, the same vertical-grid distribution is used for all models, so only horizontal interpolation is required. As in the coarse-model case, the interpolation of higher-order derivatives is used, but in this case, the original field is divergent, so that velocity potential and divergence must be used in addition to streamfunction and vorticity in order to describe the horizontal wind fields. Also, divergence as well as vorticity is interpolated, and a second Poisson equation is solved for the velocity potential on the finer grid before the divergent horizontal wind field can be reconstructed.

The potential temperature field is transferred to the finer grid using the Laplacian $\nabla^2\theta$ as the variable to be interpolated in addition to θ. The final interpolated field of θ is then obtained from a Poisson equation in which the interpolated form of the Laplacian is used as the forcing function. As in the coarse-model initialization, only a smaller interior portion of this domain is used for the final mesoscale field.

An additional task for this initialization procedure in the present case is to incorporate the observed

[6] The exception to this is that the barotropic wind field is geostrophically balanced with the barotropic pressure as will be discussed below and in Appendix B.

TABLE 1. Conditions for the four solutions to be compared.

Case	Moisture condition	Eddy viscosity treatment
ML (control)	Observed moisture	$\nu_0^v = 5$ m^2 s^{-1} in free atmosphere increasing to 20 m^2 s^{-1} at ground within surface layer ($z < 2$ km)
DL	Dry	$\nu_0^H = 10\,000$ m^2 s^{-1}
MH	Observed moisture	$\nu_0^v = 20$ m^2 s^{-1} over entire atmosphere
DH	Dry	$\nu_0^H = 40\,000$ m^2 s^{-1}

moisture field into the fine-grid initial data. This is required since the coarse (246 km) model was run without moisture included. Therefore, the observed relative humidity field is included in the coarse model data set prior to interpolation to 61.5 km grid.

A summary of the initialization procedures for both the coarse and nested-model data is presented in Appendix B.

3. Description and comparison of solutions

The synoptic situation studied here was chosen as a typical baroclinic system with moderate frontogenetic activity, as often occurs during the spring over the southeastern United States. This particular case was selected because the frontal dynamics involved seem to have been unaffected by complicating orographic effects. In addition, an intense secondary convective system was observed to develop during this period in the form of a squall line in the warm sector ahead of the front. This case thus provides us with an opportunity to simulate the frontogenetic dynamics of a frontal system over relatively flat terrain as well as the propagation and interaction of a cold front with associated moist convection.

The synoptic situation occurred during the period 1200 GMT 1 May to 1200 GMT 3 May 1967 and was characterized at 500 mb by a nearly stationary low-pressure system over the north-central United States which intensified during the first 24 h of the period. The associated trough moved from the southwest to the southeastern United States during this time. The surface low, initially located over South Dakota, moved northeastward into Quebec during the first 24 h. The associated cold front, extending from the Great Lakes to south Texas at the initial time, was part of an occluded system reaching into southern Canada. In the warm sector east of this front, skies were overcast, with squall lines developing intermittently parallel to and ahead of the front over the southeastern United States. During this period, the frontal system traveled southeastward to a position off the east coast after 48 h, at 1200 GMT 3 May.

Gridded NMC data were used to provide initial and boundary conditions for a coarse (246 km grid) dry numerical solution over the 48 h period beginning 1200 GMT 1 May 1967. This solution was then used to produce initial and boundary data (in the manner described in Section 2e) for four different fine-grid solutions which are identical to each other except for differences in eddy-viscosity magnitudes and moist/dry initial conditions as described below and summarized in Table I.

The four model configurations will each be designated by a two-letter symbol. The moisture conditions will be denoted by the first letter where D and M will be used to indicate dry and moist conditions respectively. In the moist cases, the observed moisture field used in the initial and boundary conditions was taken from the NMC data set. The water vapor mixing ratio at the surface in these cases is determined by prescribing a relative humidity of 60% over land and 85% over water (as described in Section 2d). Clearly the use of this simplified surface-moisture condition will affect the timing and intensity of the convection in the solution. However, our purpose here is to study the interaction of this convection with the frontal circulation rather than to produce a detailed prediction of convection events.

The eddy-viscosity treatment is indicated by the second letter in the symbol designation. Specifically, the letter H will denote the high-viscosity case in which the minimum or background vertical eddy viscosity, ν_0^v, is 20 m^2 s^{-1} over the entire depth of the atmosphere. The letter L will designate the low-viscosity case where ν_0^v is only 5 m^2 s^{-1} in the free atmosphere above a surface layer 2 km thick, in which ν_0^v increases to 20 m^2 s^{-1} for $z < 1$ km. The ratio of horizontal to vertical eddy viscosities is constant with height in both cases with a value of 2000. The minimum horizontal eddy viscosity ν_0^H thus assumes values of 10 000 and 40 000 m^2 s^{-1} for the low (L) and high (H) viscosity cases respectively.

Table 1 summarizes the differences among the four cases studied here. Special attention will be given to the more realistic low-viscosity, moist solution ML, which will be used as a control solution when comparisons are to be made between cases.

Finally, before proceeding to a comparison of solutions, we first introduce the horizontal smoothing operator to be used. This operator is used extensively in the analysis presented in Sections 3b and 3c as a method for filtering finer scale features so that we may separate meso-α effects (with horizontal scales $L \sim$ 250–2500 km) from meso-β effects (with L

~ 25–250 km). The basic solutions were all produced on a fine mesh 38 × 30 horizontal grid with $\Delta x = \Delta y = 61.5$ km. To obtain a smoothed version of each solution, which we refer to as the "meso-α" version, we average each field from the fine-grid solution back to the coarse-grid mesh where $\Delta x = \Delta y = 246$ km, thereby producing a four-fold reduction in horizontal grid resolution. This smoothing is done by a straightforward area-weighted averaging procedure. In this method, the value of a variable located at a grid point (x_f, y_f) on the fine grid is viewed as representing the magnitude of that quantity over the rectangular area defined by the boundaries $x = x_f \pm \Delta x_f/2$, $y = y_f \pm \Delta y_f/2$. Therefore, the smoothed value of the quantity defined on the coarse grid at the point (x_c, y_c) is found by taking the area-weighted average of the values of all fine grid points which lie within the coarse-grid box, the boundaries of which are $x = x_c \pm \Delta x_c/2$, $y = y_c \pm \Delta y_c/2$.

The resulting meso-α variables, as well as the smoothed solutions taken as a whole, will be denoted by angular brackets; therefore, for example, the smoothed form of the potential temperature, θ, from case ML will be referred to as $\langle\theta\rangle$ while the smoothed version of solution ML taken as a whole will be denoted as $\langle$ML$\rangle$. The smoothed fields on the coarse 246 km grid will also be linearly interpolated back to the fine 61.5 km grid in Section 3c. This is required so that meso-β features may be displayed directly as the difference between the original and the smoothed fields.

Comparison with observations

The constant pressure charts for gridded NMC observations will be compared with the fine control solution, ML, and its coarse smoothed version, $\langle$ML$\rangle$, which has the same resolution as the gridded observational data ($\Delta x = 246$ km). Four standard pressure levels, 1000, 850, 500 and 300 mb, are presented in Figs. 2–5, respectively. A time sequence at 12 h intervals is shown in each figure for geopotential height, temperature, and wind, with conventional wind flags used to indicate wind direction and speed (in knots). The observational fields shown in the top row of each figure correspond to the coarse-model domain with the region encompassing the fine model domain designated by the interior boxes in these upper charts. Although ML was run to 48 h (1200 GMT 3 May 1967), only the first 36 h are shown in Figs. 2–5 because of space limitations. Solutions at 48 h will be shown in later sections.

The 1000-mb fields shown in Fig. 2 also contain the position of the surface front and the areas of precipitation as it occurred in the observations and in the model over the previous 6 h. In the observations, the frontal positions and the precipitation areas were obtained from surface analyses rather than from the gridded data set. The position of the front in the numerical results was determined as the line of maximum vertical vorticity (referred to below as the vorticity band) in the frontal region.

The model shows good success in correctly following the motion of the observed front and low pressure system over the duration of the integration. Although the low occurs along the northern boundary (with the center of the depression outside of the domain), its behavior is only partially controlled by the prescribed boundary conditions. (Specifically the boundary region to the east of the pressure trough is outflow; baroclinic variables on this boundary will thus be extrapolated from the interior rather than be determined by external boundary values.) As the low-pressure system moves eastward, a high pressure system moves into the northwest portion of the model domain; however, the southerly flow near the western boundary in the observations at 1200 GMT 2 May and 0000 GMT 3 May becomes an easterly flow in the simulation. The southerly flow in the observations is apparently caused by the mountains to the west; therefore, because the model does not contain orography, the flow about the high located in the northwest moves directly westward without this orographic impediment.

The wind intensity along the front in Fig. 2 is somewhat stronger than that in the observations; the wind direction is quite similar ahead of the front but is more normal to the front than observations indicate on the cold air side at 12 h and 24 h. The overall temperature gradients are well simulated in the eastern part of the model, whereas mountain effects in the west produce distortions similar to those in the geopotential field.

The circulation at 850 mb (Fig. 3) shows similar features to that at 1000 mb with the mountain effect in the west causing the major disparity in wind and temperature. The winds in the southeast are very close to the observations in both direction and speed. The low-pressure system in the north is reasonably simulated in its position and intensity, but the north–south gradient of geopotential height is weaker than observations show.[7] This bias can even be seen in the initial field.

The diurnal effect is only included in the model insofar as it influences the boundary data. If this

[7] The persistent bias in the geopotential height of 100 m at 1000 mb between the observations and the model results is attributable to two effects, *viz.*, our choice of the reference value θ_0 to be 328 K, and a small constant disparity which exists in the barotropic pressure boundary values for (2.18). This constant bias has no dynamical significance in the solution because it does not alter the horizontal pressure gradient.

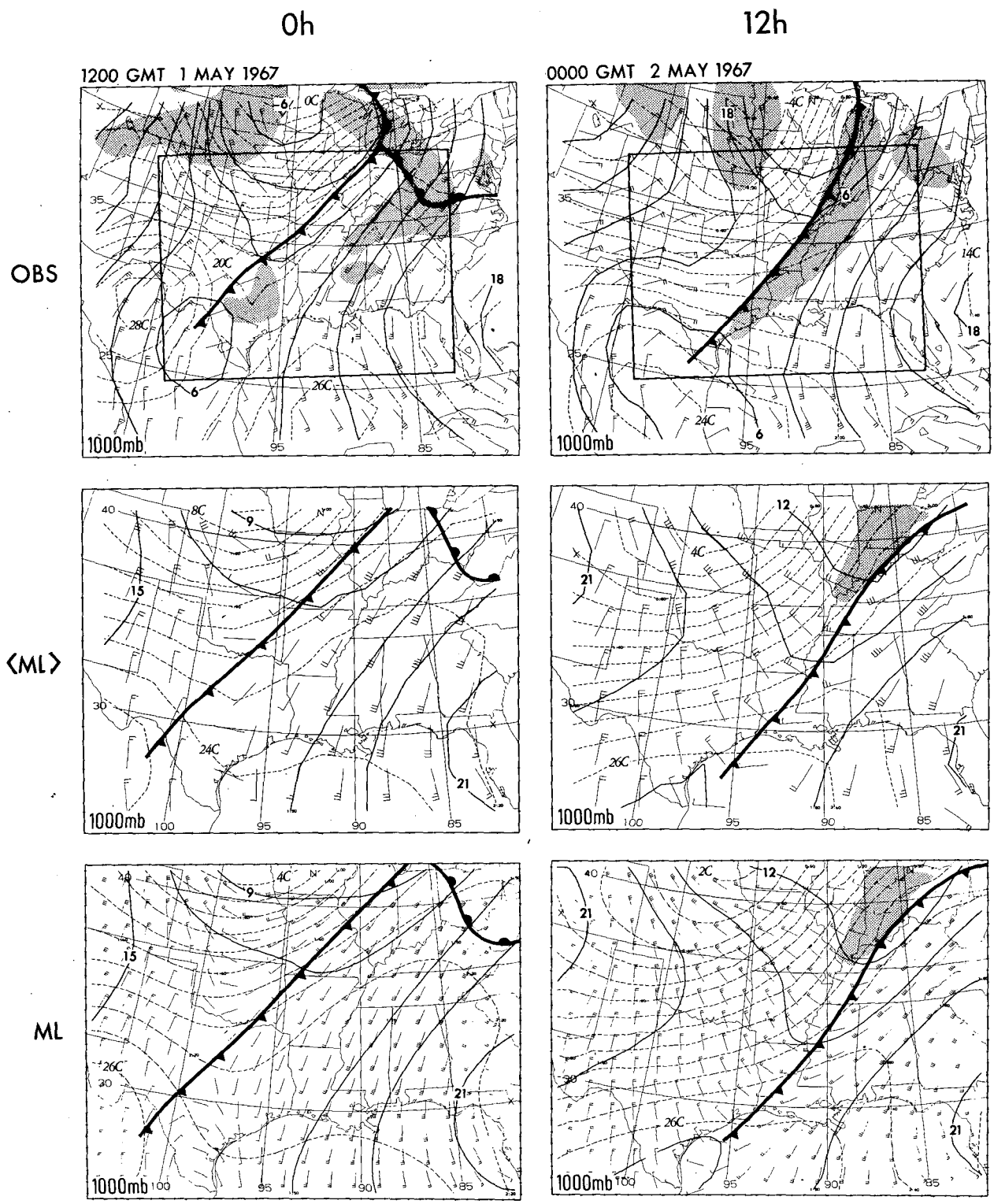

FIG. 2. Charts on the 1000 mb constant pressure surface at 12 h intervals for (i) observed fields on the coarse model grid (top row), (ii) solution ⟨ML⟩ which is smoothed to coarse grid points (middle row), and (iii) unsmoothed fine grid solution ML (bottom row). Solid lines indicate geopotential heights labeled in tens of meters. Dashed lines denote temperature in °C. Wind barbs indicate wind direction and speed in knots according to standard meteorological convention. The border of the fine model domain is marked by a box in the upper frames. The positions of the surface fronts are indicated. Also regions in which precipitation was measured at the surface during the preceeding 6 hours are indicated by stippling.

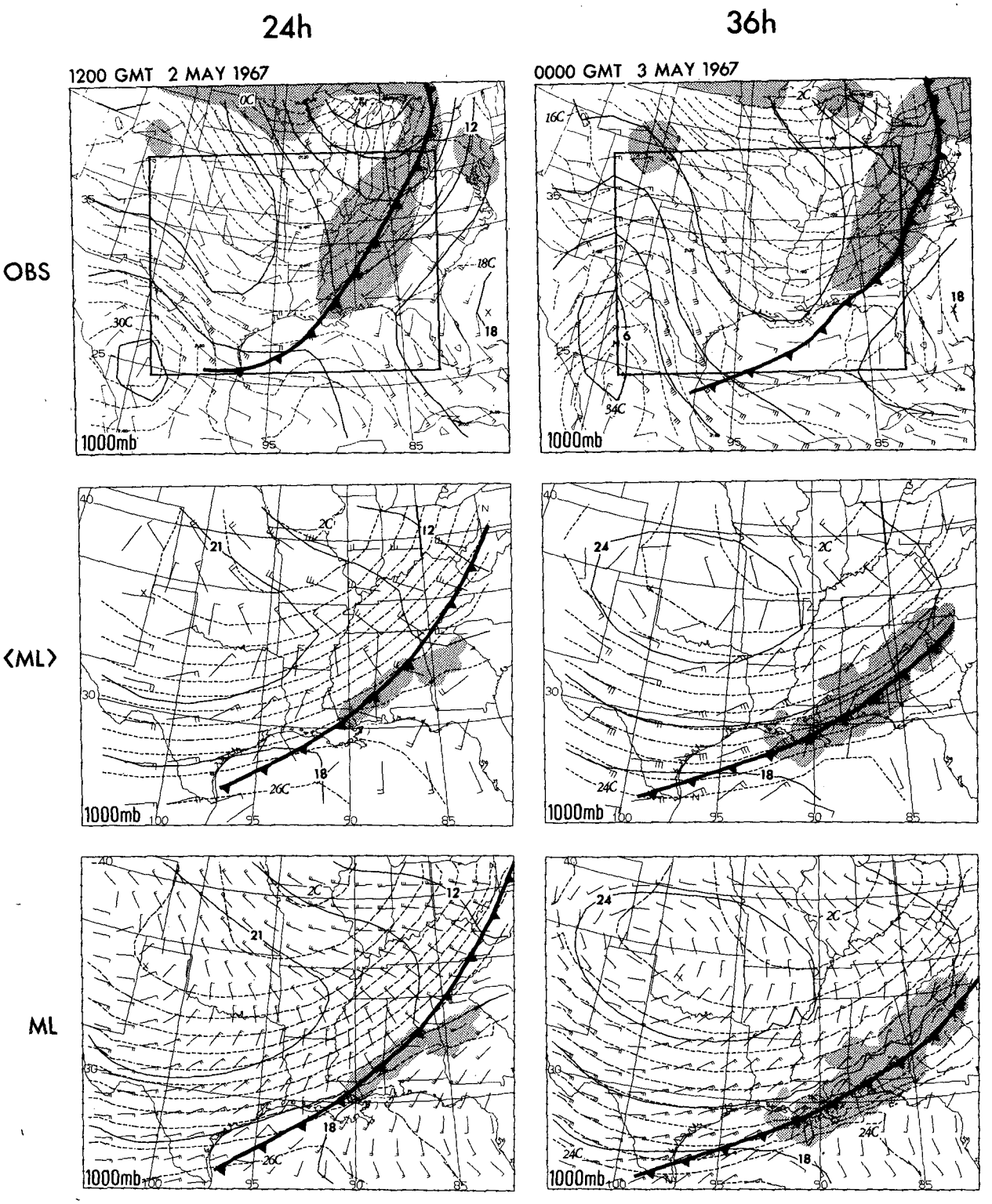

FIG. 2. (*Continued*)

diurnal variation is important in the present case, it should appear as changes in low-level observed fields such as the 1000- and 850-mb winds over the Plains; these changes would be largely absent from the model, thereby producing discrepancies between the solution and observations. The fact that the differ-

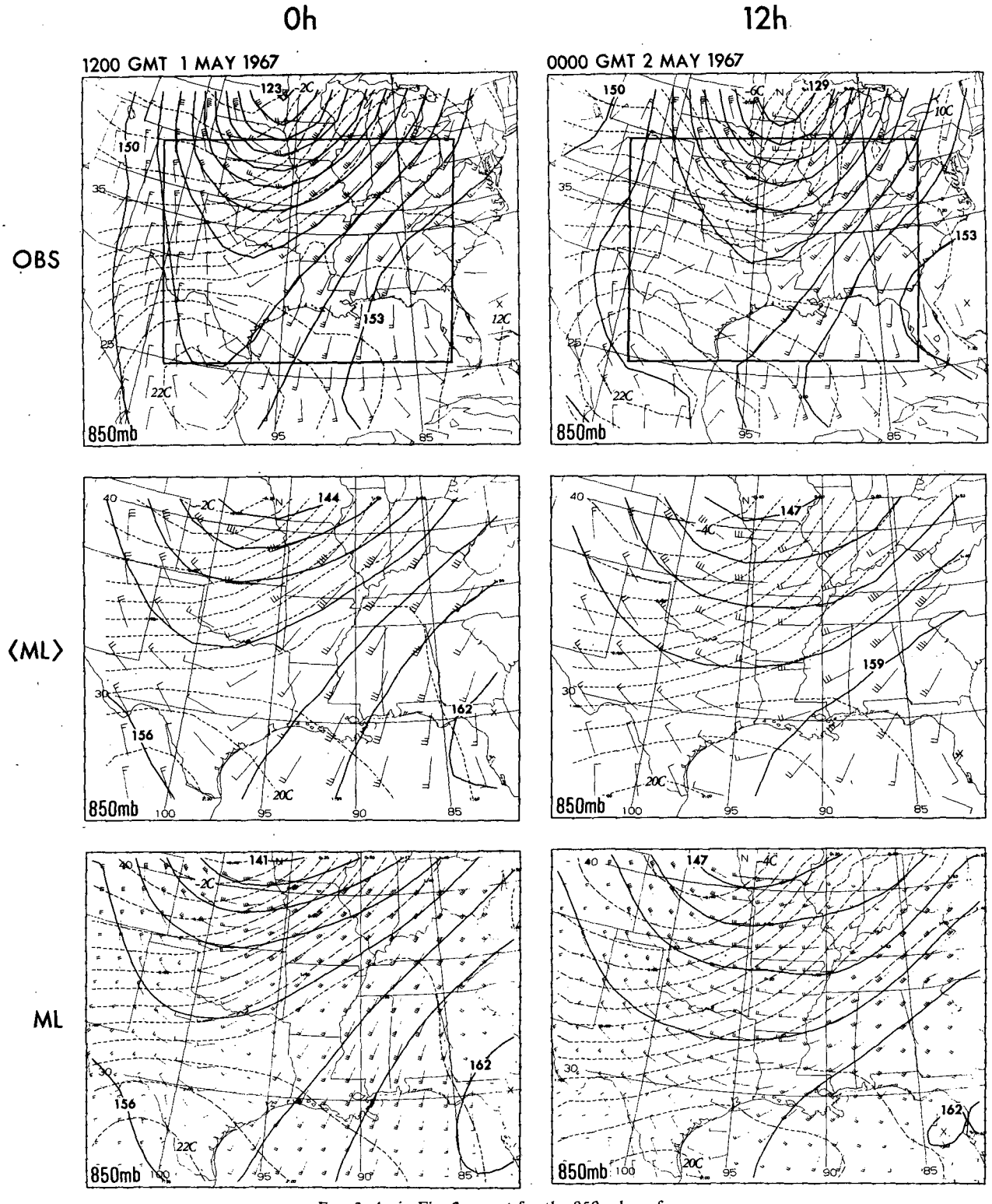

FIG. 3. As in Fig. 2 except for the 850 mb surface.

ences found in the low-level winds of Figs. 2 and 3 are quite independent of the day–night cycle suggests that diurnal influences upon the solution are small.

A mesoscale circulation is apparent in the southeast corner of ML in Fig. 3 at 0000 GMT 3 May. This small-scale disturbance is clearly due to the deep convection occurring in the solution at this time above the surface front. Note that neither the observations nor ⟨ML⟩ indicate this detailed feature.

For the upper level fields at 500 and 300 mb (Figs.

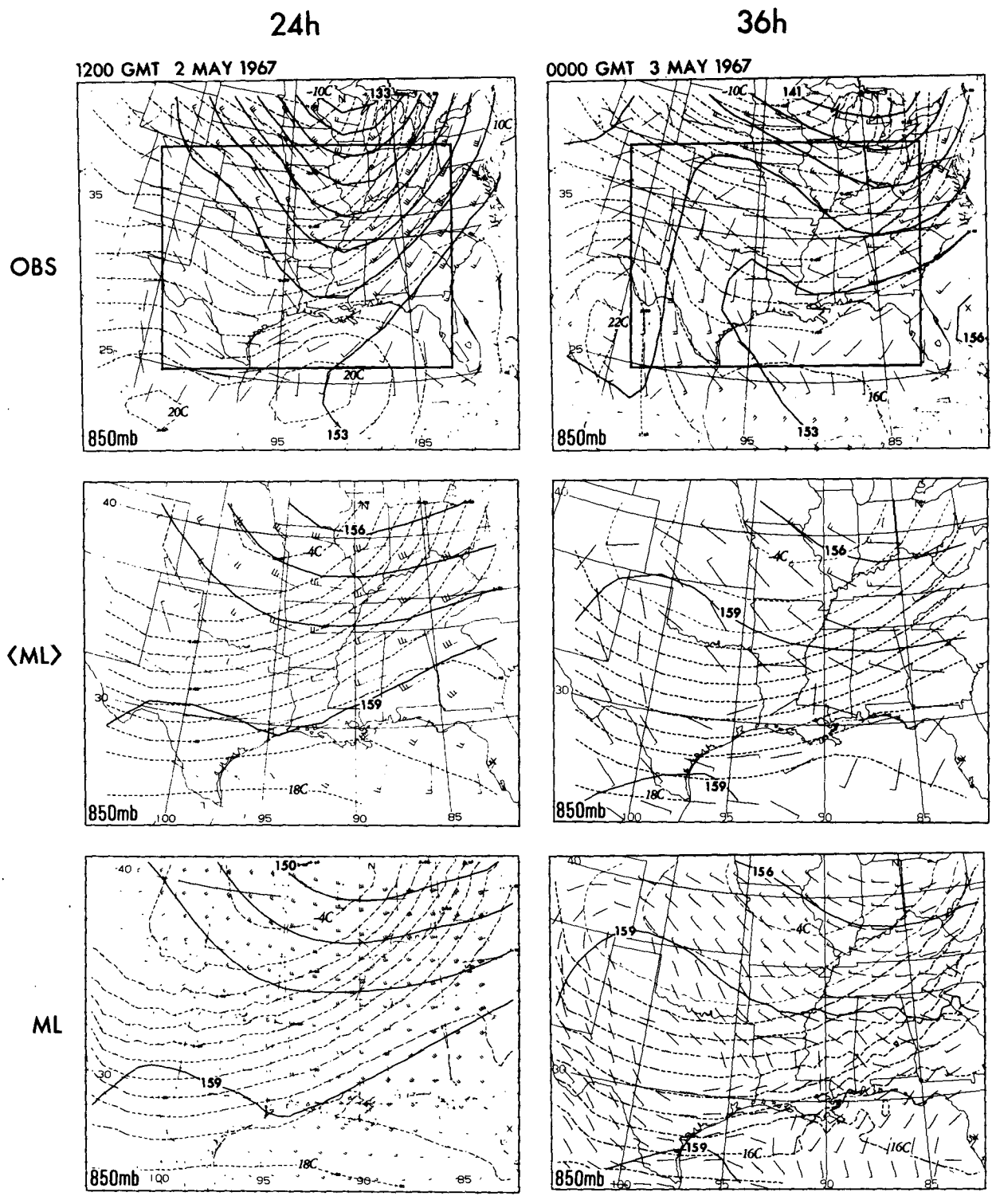

FIG. 3. (*Continued*)

4 and 5), the large discrepancies found in the low levels are absent[8] and the observed features are modeled quite well. Note, however, that the jet intensity in the solution at both 500 and 300 mb is consistently high by 10 knots (5 m s^{-1}) compared to the observed values. At 500 mb, the observations for 1200 GMT 2 May show a maximum wind of 70 knots (36 m

[8] However, as Section 4 will show, derivative quantities such as divergence may differ at these levels due to effects such as a change in the intensity or location of the outflow above a convective zone.

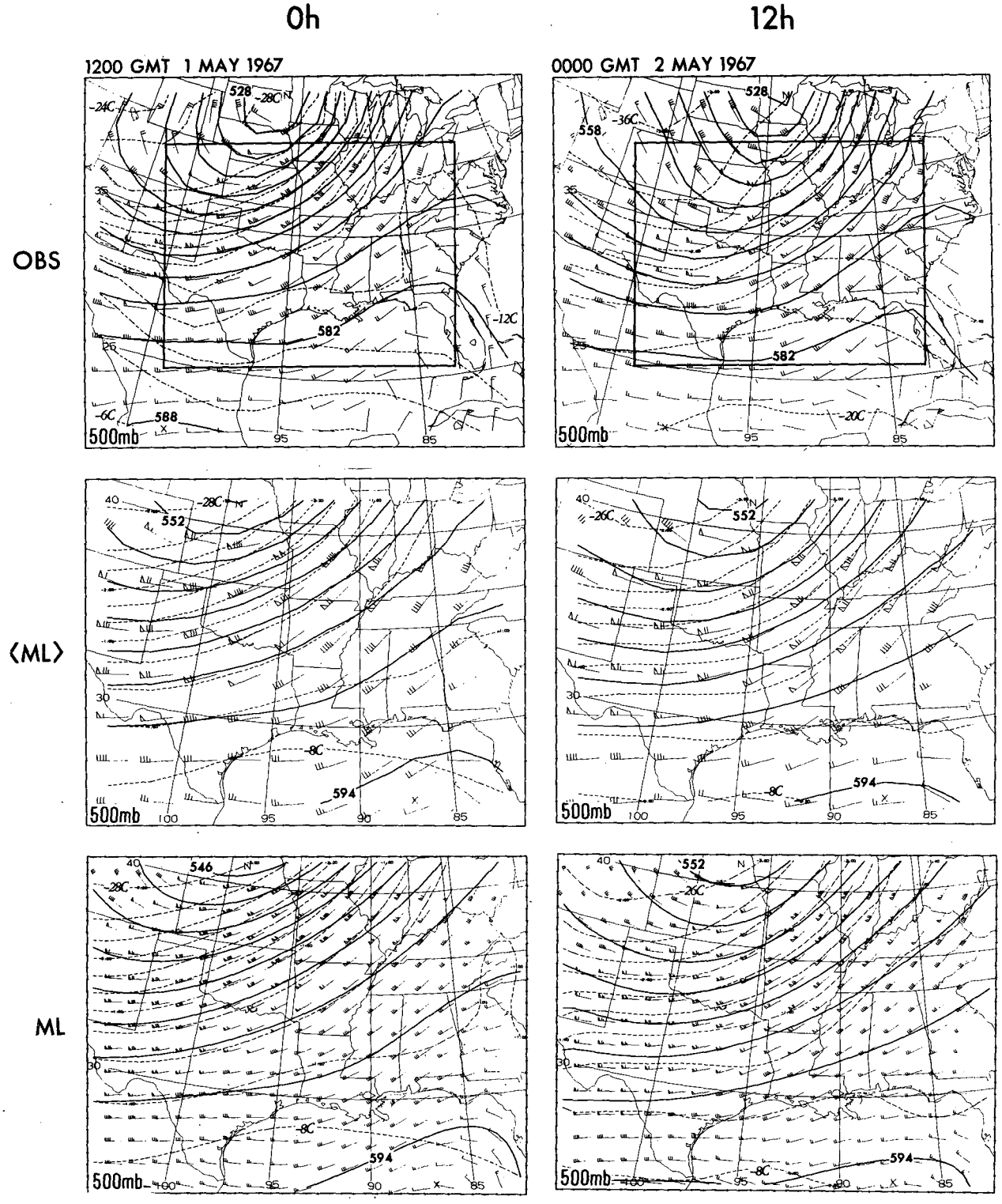

FIG. 4. As in Fig. 2 except for the 500 mb surface.

s^{-1}) whereas the model solution indicates 80 knots (41 m s^{-1}). Similarly, at 300 mb, the wind maximum of 90 knots in the observed field is increased to 100 knots in the model.

4. Meso-α features

The dependence of the four solutions shown in Table 1 on eddy viscosity and humidity will be in-

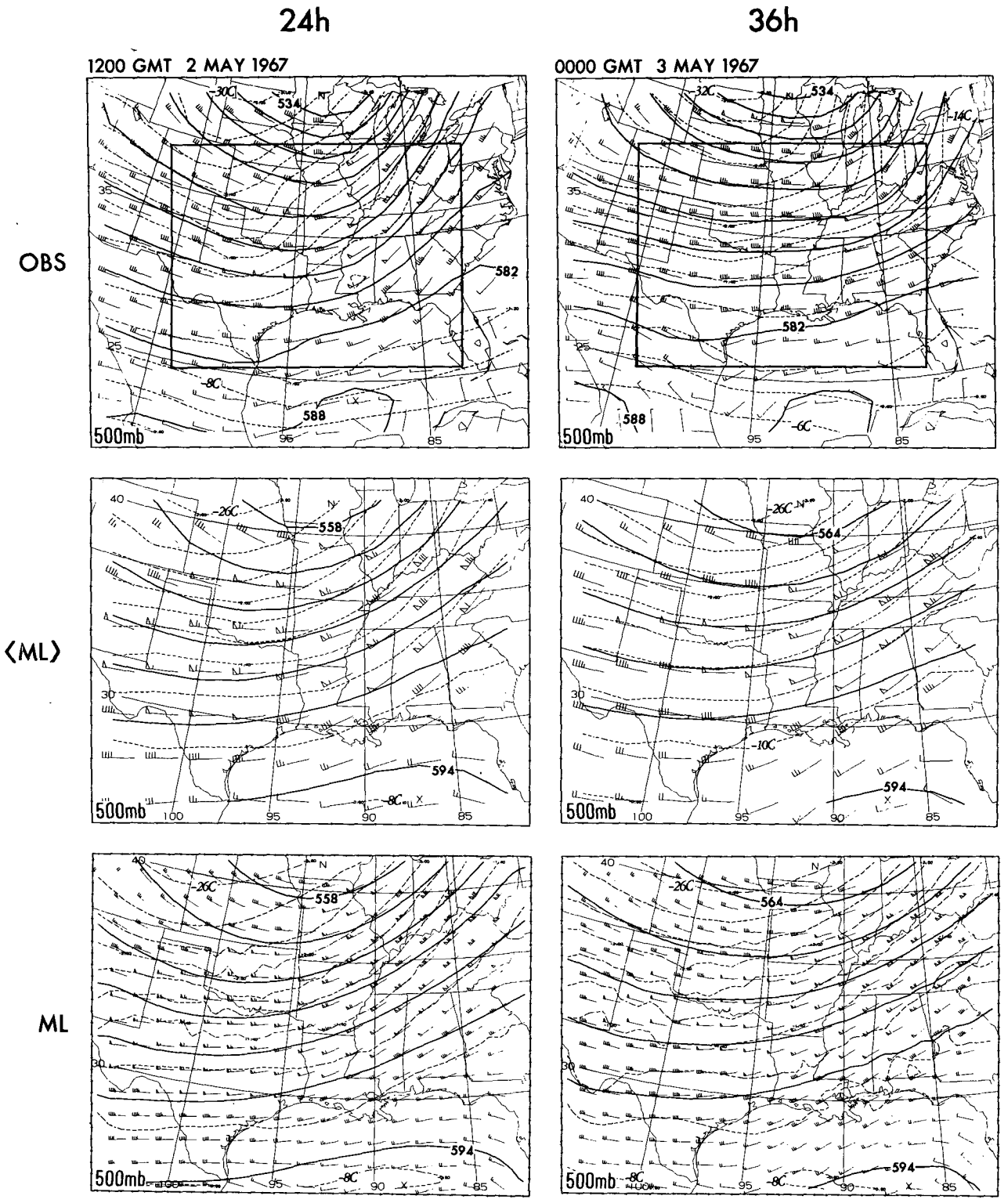

FIG. 4. (*Continued*)

vestigated in this and the following section using the smoothing operator to distinguish "meso-α" and "meso-β" features. In the present section, we will look at the meso-α differences between the three cases MH, DL, and DH and the more realistic control solution ML by comparing the coarse-grid differences $\langle MH \rangle - \langle ML \rangle$, $\langle DL \rangle - \langle ML \rangle$, and $\langle DH \rangle - \langle ML \rangle$ for different times and heights. Then, in

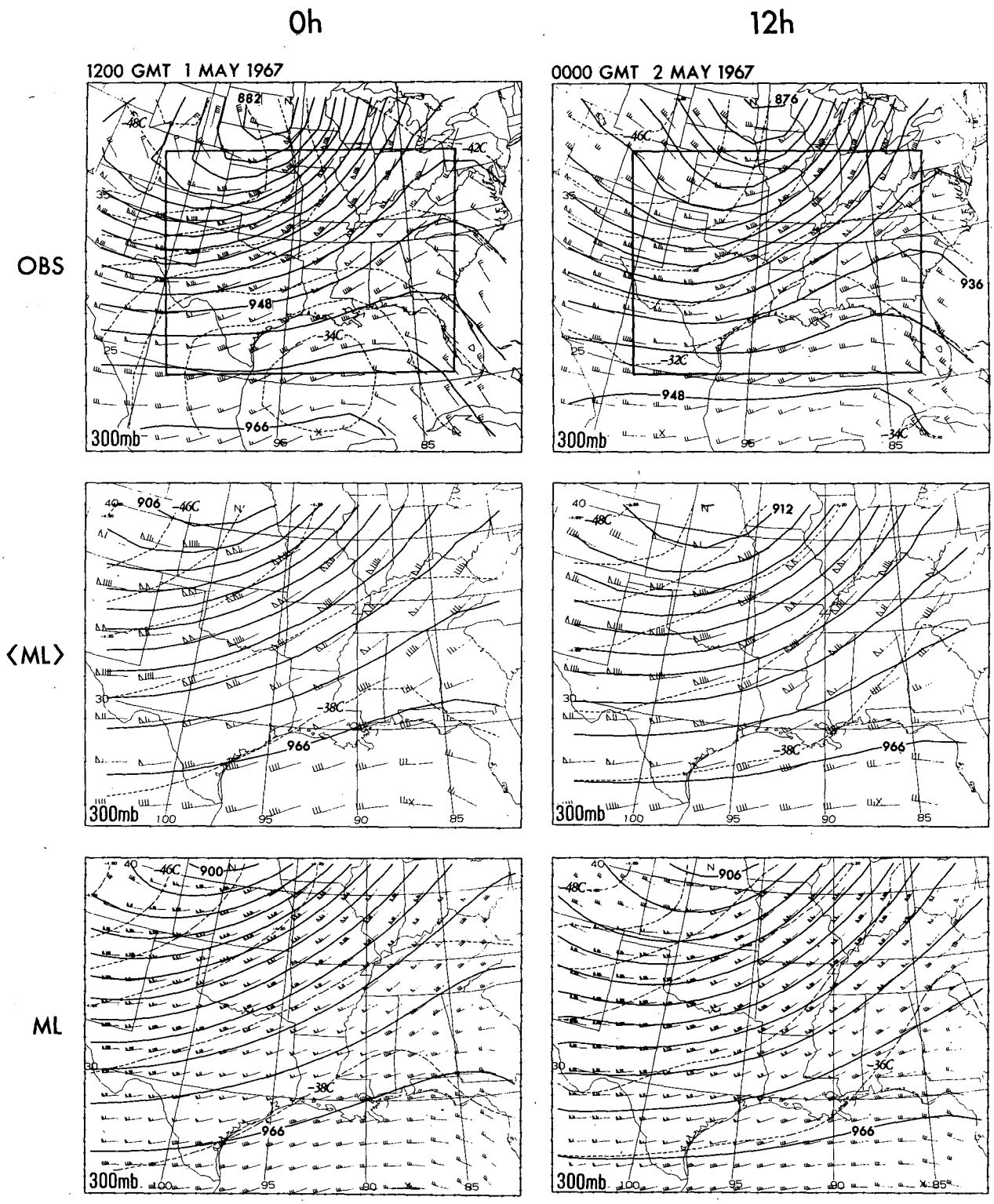

FIG. 5. As in Fig. 2 except for the 300 mb surface.

the next section, we will try to isolate the smaller meso-β features by comparing the fine-grid solutions including temperature difference fields for ML − ⟨ML⟩, MH − ⟨MH⟩, and DL − ⟨DL⟩. In the figures which follow, plots will be presented for constant height levels which roughly correspond to the standard pressure levels treated in the previous section. In particular, model levels will be displayed for

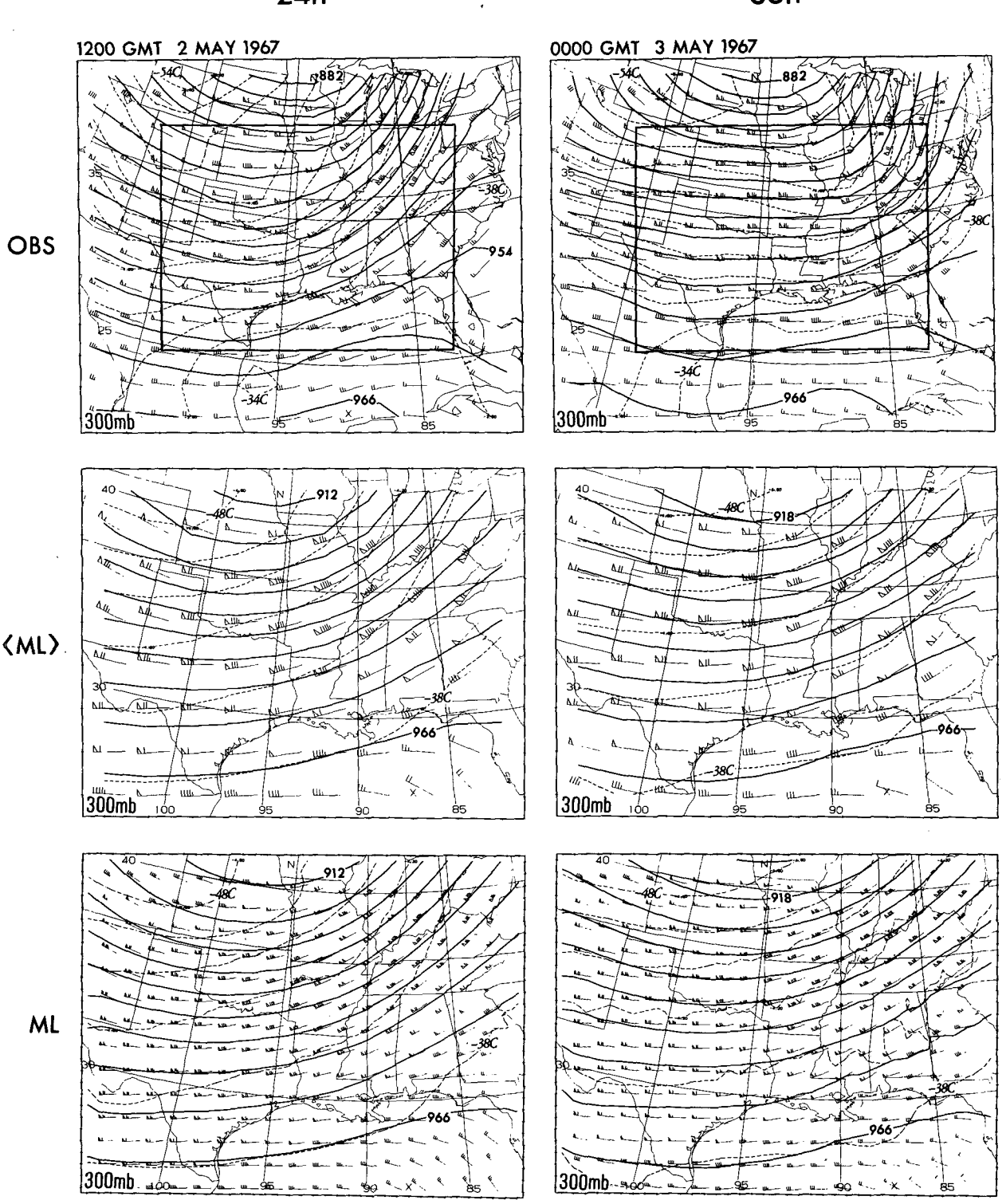

FIG. 5. (*Continued*)

heights of 0, 1500, 5500, and 9500 m (which roughly correspond to 1000, 850, 500 and 300 mb, respectively).

Fig. 6 shows composite plots of the lower three levels for the control case ⟨ML⟩ at 24 and 48 h. The averaged fields for pressure (solid contours), poten-

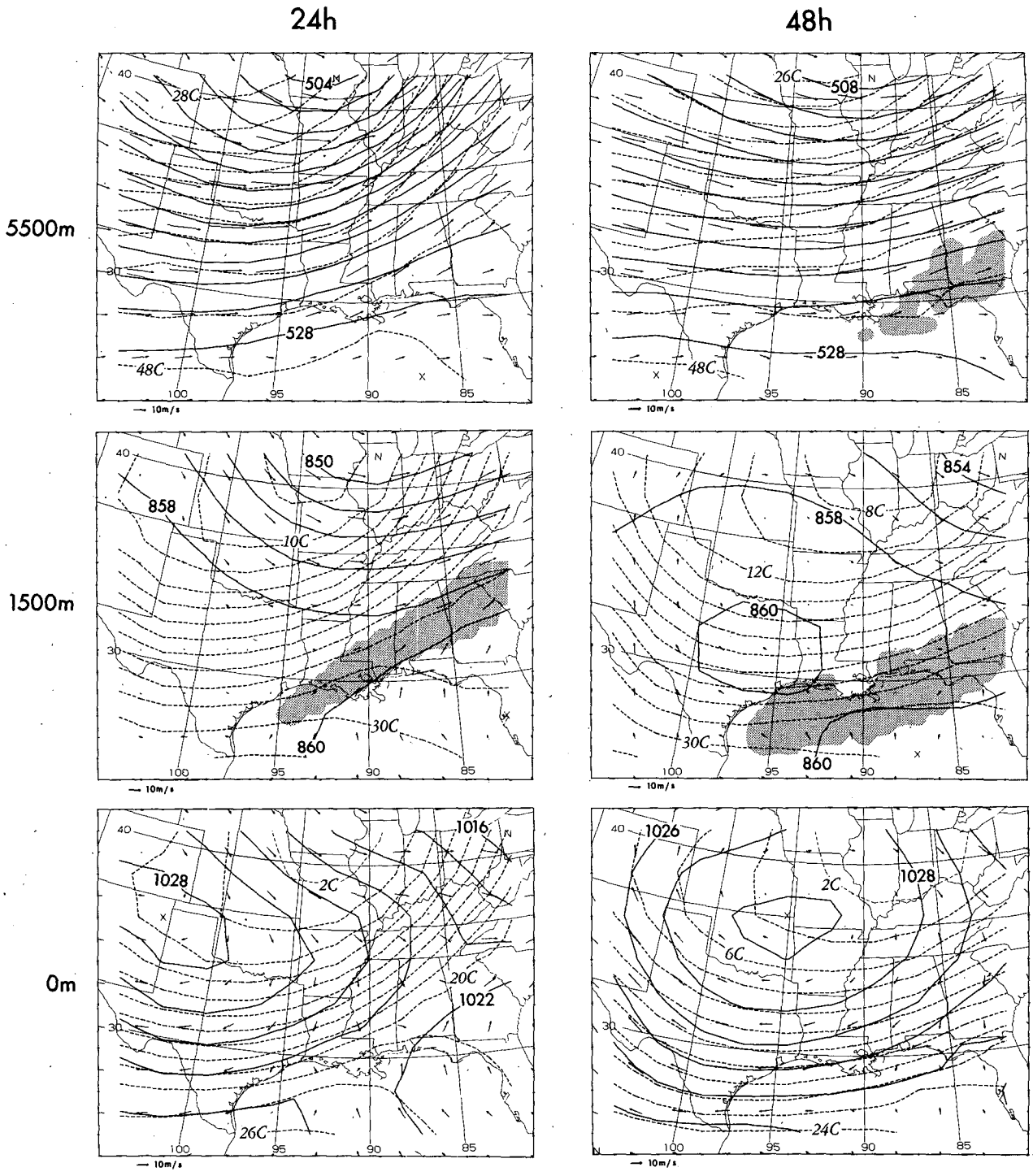

FIG. 6. Contour plots of smoothed control solution ⟨ML⟩ at 24 h and 48 h for constant height levels z = 0, 1500, and 5500 m. Pressure (in mb) and potential temperature (in °C) are denoted by solid and dashed contours, respectively. Vectors indicate horizontal winds with the magnitude scaled relative to the length for 10 m s^{-1} as shown below the southwest corner of each frame.

tial temperature (dashed), and horizontal winds (vectors)[9] are shown in this figure as a reference for their corresponding difference fields in Figs. 7–9. The cloud zones (indicated by stippling) are determined by the complete, unsmoothed cloud fields of ML in order to indicate regions of moist convection in the solution.

The cloud patterns in Fig. 6 demonstrate that con-

[9] Vectors will be used throughout this paper to denote wind direction and speed except in Section 3a where wind flags are used in the constant pressure plots.

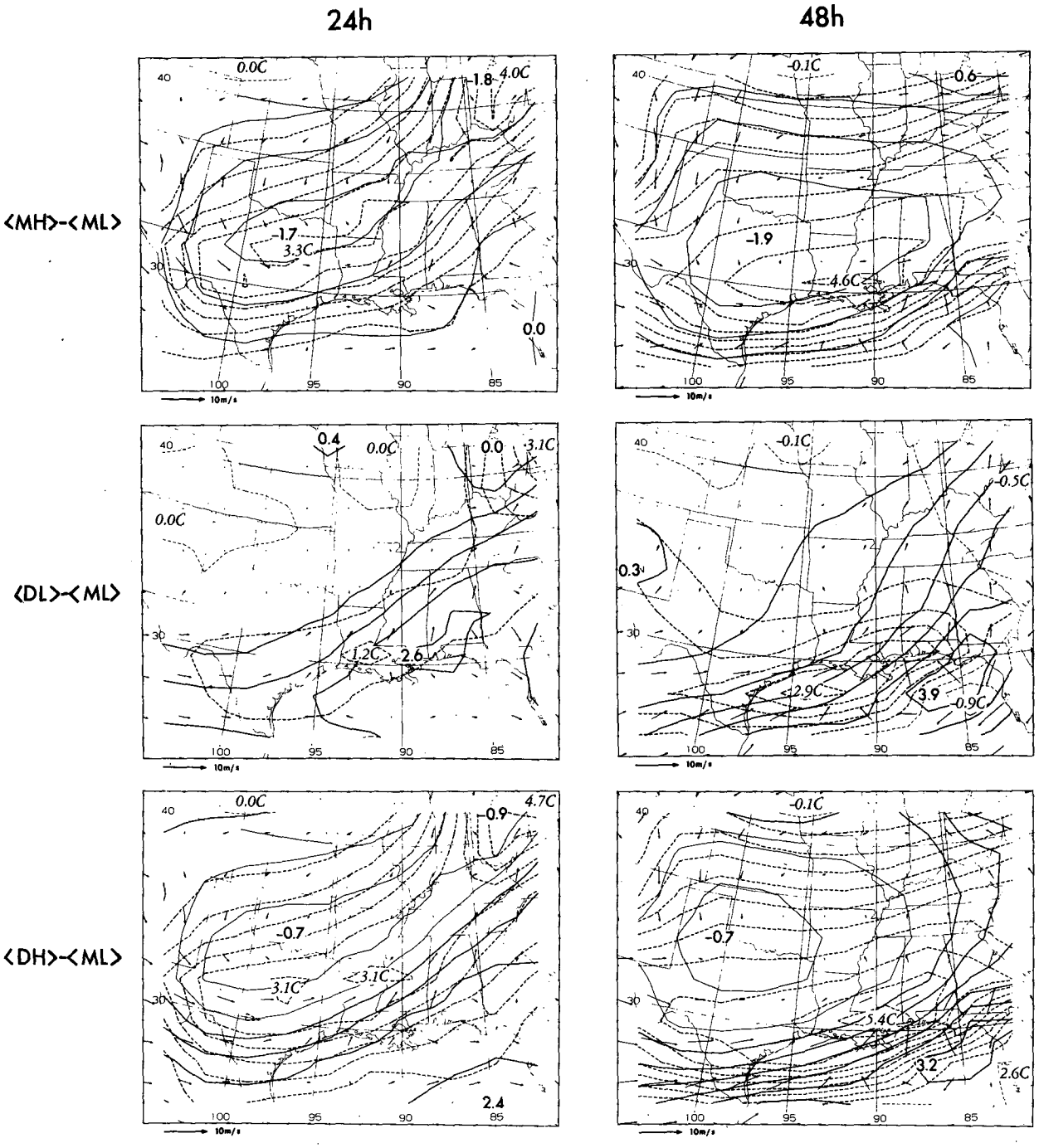

FIG. 7. Plots of pressure difference in mb (solid contours), potential temperature difference in °C (dashed contours), and horizontal velocity difference (vectors, scaled by 10 m s^{-1} vector at lower left of each frame) for height level $z = 0$ m at 24 and 48 h. All differences are computed between the smoothed solutions ⟨MH⟩, ⟨DL⟩, and ⟨DH⟩ and the smoothed control solution ⟨ML⟩.

vection is only beginning to develop at 24 h with a shallow line of convection occurring at $z = 1500$ m along the frontal zone. On the other hand, the cloud patterns at the end of the calculation (48 h) indicate deep convective penetration, shown in Fig. 10 to extend above 9500 m. It is therefore convenient in this section to discuss the meso-α differences at 24 and 48 h as indicative of the larger-scale features of the solutions during two separate phases. The fields at 24 h do not involve significant diabatic heating effects but rather are dominated by synoptic-scale dynamics. The moist air parcels above the front have still not been lifted sufficiently to achieve free convection. During the ensuing 24 h, however, the unstable convection which develops becomes sufficiently intense within this area that it not only

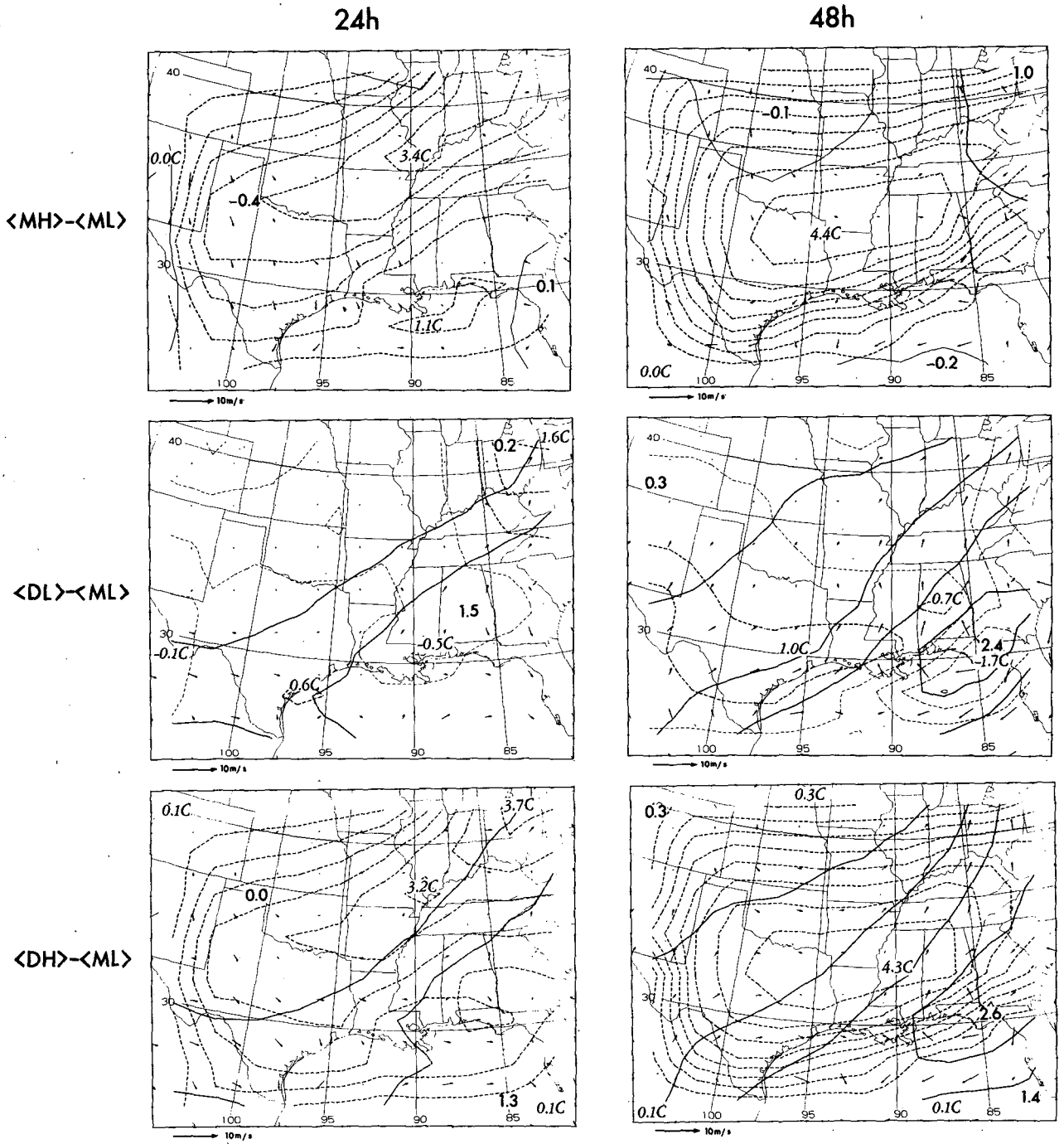

FIG. 8. As in Fig. 7 except for level z = 1500 m.

dominates the meso-β dynamics but also alters many features of the larger meso-α scales, as indicated in the following discussion.

In the surface difference fields shown in Fig. 7, two effects predominate at 24 h. (A third feature, namely the disturbance in the northeast corner of the domain, is apparently numerical in its origin and is discussed below.) First, the increased diffusion coefficients used in cases MH and DH (see Table 1) are shown to slow the southeastward movement of the frontal system when compared with the low-viscosity control case, ML (and the associated dry case, DL). As a result of this effect, a large region of positive temperature difference develops in the fields for $\langle MH\rangle - \langle ML\rangle$ and $\langle DH\rangle - \langle ML\rangle$ by 24 h, with maximum anomalies of 3.1–3.3°C occurring near the

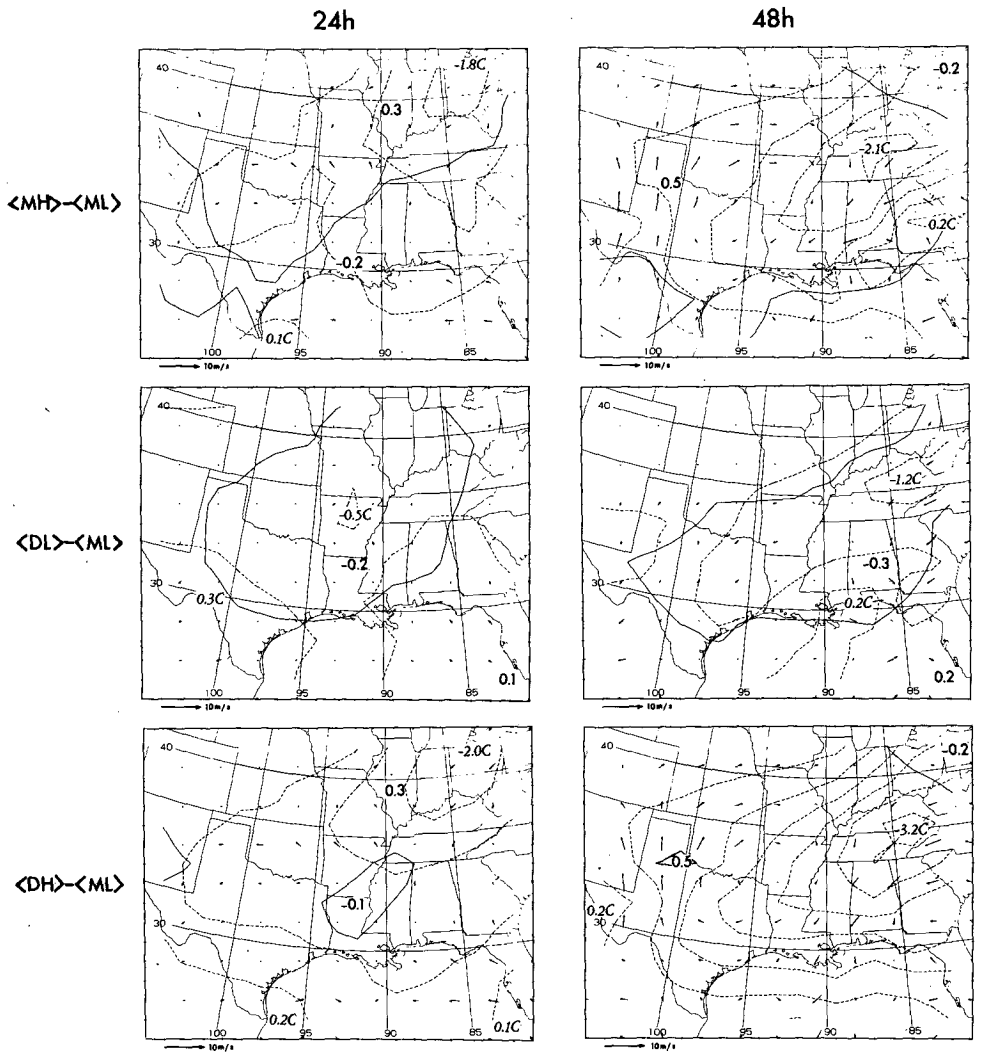

FIG. 9. As in Fig. 7 except for level z = 5500 m.

center of the domain in the area of largest horizontal temperature gradient. This anomaly implies a southward displacement of the frontal system in ML of roughly 100 km as compared with MH and DH.

The pattern of negative pressure difference, Δp, in $\langle MH \rangle - \langle ML \rangle$ is seen to correspond closely with the above $\Delta\theta$ pattern; the minimum Δp of -1.7 mb occurs at the same point as the $\Delta\theta$ maximum. The vector differences, ΔV, which have developed by 24 h seem to be adjusting geostrophically to the pressure difference field.[10]

The second important effect which is evident at 24 h is the pressure difference which occurs in the dry cases, DL and DH, due to the absence of water vapor. In particular, the hydrostatic pressure at any point in the moist cases, ML and MH, will be reduced compared to their dry counterparts in proportion to the total water vapor content of the air column above that point. This effect largely explains the pressure difference pattern for $\langle DL \rangle - \langle ML \rangle$ at 24 h where Δp is as large as 2.6 mb in the moist air ahead of the front but decreases across the frontal zone to a value of <1 mb behind the front. The increased pressure gradient which occurs in $\langle ML \rangle$ as compared to $\langle DL \rangle$ leads to an increase in the surface winds along the front by as much as 3 m s^{-1}; this velocity increase is therefore attributable to the presence of water vapor and its effect upon the pressure.

In view of the above discussion, the differences for $\langle DH \rangle - \langle ML \rangle$ represent the combined effects of increased diffusion and the absence of water vapor in DH at 24 h. Thus a broad positive temperature region is evident over much of the domain because

[10] As the reference vector in the lower left corner of each map indicates, vector lengths in Figs. 7–10 for a given differenced wind magnitude are four times as large as they are in Fig. 6 for an equivalent undifferenced wind.

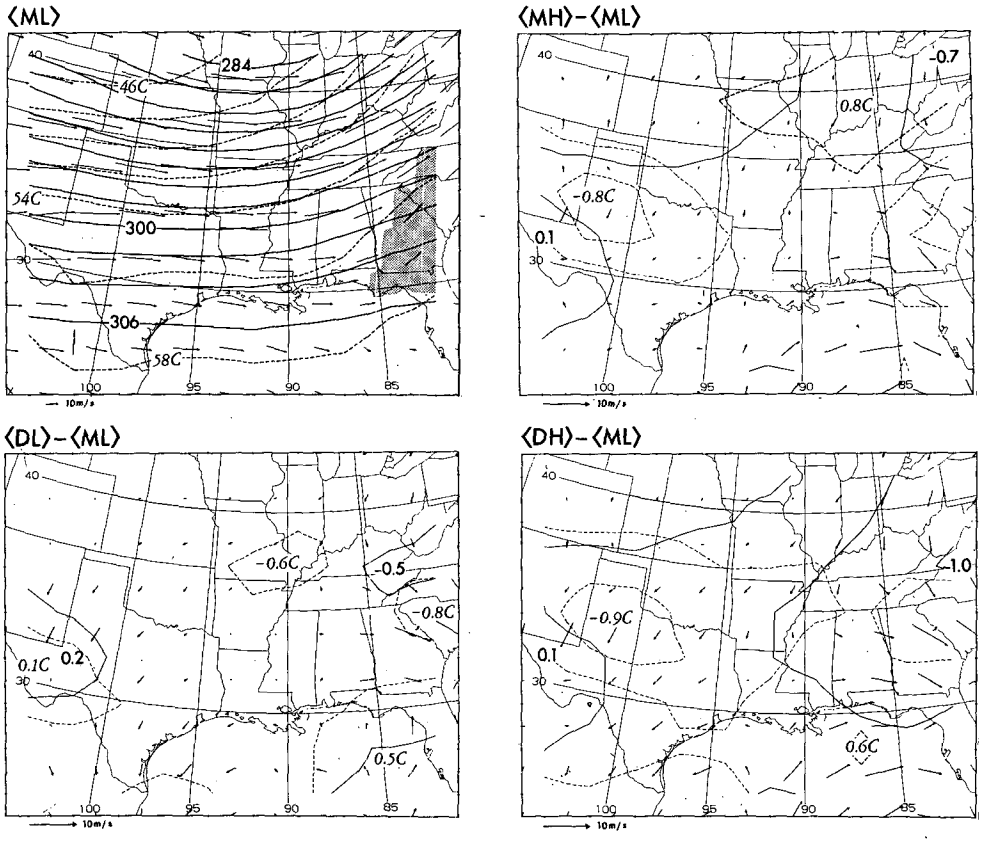

FIG. 10. Composite for level z = 9500 m at 48 h showing smoothed, undifferenced fields of ⟨ML⟩ in upper left frame (as in Fig. 6) and difference fields for ⟨MH⟩, ⟨DL⟩, and ⟨DH⟩ relative to ⟨ML⟩ in other three frames (as in Figs. 7–9). Vector lengths in the difference plots are four times as large as they are in the undifferenced plot in the upper left frame.

of viscous retardation of the frontal movement, while the accompanying negative pressure field has been weakened and shifted relative to ⟨MH⟩ − ⟨ML⟩ as a result of the influence of water vapor on pressure.

Finally, a localized disturbance may be seen in the northeast corner of the domain as a positive temperature difference in the low-viscosity case ⟨DL⟩ − ⟨ML⟩ and to a lesser extent in the two high-viscosity cases where it appears as part of the frontal shift. This feature is only evident around 24 h and appears to be due to the interaction of the surface front with the boundary treatment as the front passes the northeast corner.

At 48 h, the effects of water vapor and viscosity are still evident but now are modified by the convection which occurs above the leading edge of the surface front (see Fig. 6). The influence of convection on the difference fields is most apparent in the dry cases and particularly for ⟨DL⟩ − ⟨ML⟩, which is not dominated by the frontal retardation evident in ⟨DH⟩ − ⟨ML⟩. The positive potential-temperature anomaly in the south-central part of ⟨DL⟩ − ⟨ML⟩ is of particular interest since it largely occurs beneath the cloud zone (the averaging operator will tend to spread anomalies relative to the unaveraged cloud zone shown in Fig. 6).

Two possible causes are apparent as mechanisms to produce this decrease in θ in the moist case ML relative to DL. First, the strong low-level convergence which is produced by the convective zone could modify the horizontal temperature advection beneath the cloud zone so as to produce increased cold advection to the south relative to the dry case DL. The difference vectors in ⟨DL⟩ − ⟨ML⟩, in fact, indicate increased southward flow in ⟨ML⟩ and therefore support such a differential advection hypothesis at 48 h (increased southward flow in ⟨ML⟩ compared to ⟨DL⟩ appears as a north-pointing vector in the figure). Such an effect is basically equivalent to an increased packing of the isentropes along the front due to the enhanced convergence in the moist case ML.

A further indication of this is the negative $\Delta\theta$ anomaly of −0.9°C which appears in ⟨DL⟩ − ⟨ML⟩ in the southeast corner of the domain. As the vector

differences ΔV show, this results from the increased northward advection of warm air occurring in ML due to the more intense convergence.

A second and related mechanism that also contributes to the decrease of θ beneath the cloud is the adiabatic cooling which results from the upward motion induced by the convection. This surface temperature decrease, which reflects the temperature decrease at 500 m because of the lower boundary condition of constant lapse rate (Section 2d), is shown by Orlanski and Ross (1982) to be correlated with regions of strong convergence. For the lapse rate in this region, a sustained upward motion of 1 cm s^{-1} occurring over a period of 24 h would be sufficient to produce the 2.9°C anomaly shown. Since local vertical velocities at 1000 m in this region are on the order of 10 cm s^{-1}, this adiabatic lifting mechanism seems very plausible.

A second feature at 48 h is the decrease in surface pressure within the convective zone of the moist case ML as compared to the dry cases, DL and DH. This apparent "meso-low" appears in the southeast corner of the difference fields $\langle DL\rangle - \langle ML\rangle$ and $\langle DH\rangle - \langle ML\rangle$ as local regions of positive ΔP with maxima of 3.9 and 3.2 mb respectively. The decrease in P in case *ML* is the result of higher temperatures within the cloud zone above 1000 meters which appear to be due to diabatic heating (see the negative temperature anomaly in this region at 1500 m for $\langle DL\rangle - \langle ML\rangle$ in Fig. 8).

Turning our attention now to the difference fields at 1500 m (Fig. 8), we see similar positive temperature anomalies at 24 h in both $\langle MH\rangle - \langle ML\rangle$ and $\langle DH\rangle - \langle ML\rangle$ due to the retarding effect of viscosity upon the front. The axis of this anomaly is now shifted to the north, reflecting the northwestward slope of the front itself. Similarly the two dry cases show an increase of pressure due to the absence of water vapor, although the magnitude of this increase is weaker at 1500 m. Finally the temperature anomaly in the northeast corner, which was quite evident at the surface, is still apparent in $\langle DL\rangle - \langle ML\rangle$.

At 48 h, the fields for $\langle DL\rangle - \langle ML\rangle$ exhibit several interesting features in the vicinity of the convective zone. Within the cloud region, the differences indicate the potential temperature in $\langle ML\rangle$ to be as much as 1.7°C warmer than for case $\langle DL\rangle$, apparently due to the latent heat release which is occurring within the cloud. Then, to the rear of the cloud, where the air is colder and drier, the temperature in $\langle ML\rangle$ is colder than in $\langle DL\rangle$, an effect attributable largely to evaporation of the rear wall of the cloud as shown by an analysis of the heat balance terms (Orlanski and Ross, 1982). The diabatic heating within the cloud seems to be responsible for the lower pressure occurring within the cloud and at the surface; but, the lower pressure in this meso-α field may also be due to the larger amount of q within the air columns in the cloud region as compared to air columns in the surrounding unsaturated air. The above features, which are quite apparent in $\langle DL\rangle - \langle ML\rangle$, are largely obscured by the frontal shift in $\langle DH\rangle - \langle ML\rangle$.

The 5500 m difference fields in Fig. 9 show a reduction in the intensity of potential temperature anomalies and a near absence of significant pressure differences. In fact, the lower levels are dominated by rather strong direct effects of moisture and viscosity changes in the form of frontal retardation, hydrostatic pressure differences due to moisture effects, and diabatic effects of condensation and evaporation. On the other hand, the upper levels, specifically the heights of 5500 m and 9500 m, are influenced by weaker, more indirect effects of viscosity and moisture changes. These changes alter the middle atmosphere through their influence upon the vertical circulation associated with the frontal system and through the effect of moisture inclusion in producing deep convection which alters the upper tropospheric flow field in the vicinity of the convective zone. Of course, this is not surprising since the primary moisture effects are confined to the lower levels where the large gradients associated with the surface front should produce the largest alteration of the solution due to changes in viscosity.

The most notable feature in Fig. 9 is the temperature anomaly which appears in both viscous difference cases, $\langle MH\rangle - \langle ML\rangle$ and $\langle DH\rangle - \langle ML\rangle$, as a tongue of negative difference, the axis of which maintains a nearly constant position and orientation relative to the surface front between 24 h and 48 h. Reference to vertical cross-sections aligned perpendicular to the surface front and the jet stream suggests that the increased temperature at this level in ML as compared to DH, MH, and DL results from the more intense adiabatic warming due to downward motion in ML beneath the jet stream. Comparison of temperature anomalies in Fig. 9 would then imply that the vertical frontal circulation is strongest in the moist, low-viscosity case, ML, and least intense in the dry, high-viscosity case, DH; in addition, the temperature for this region in DL is shown by a comparison of differences to be warmer than in MH, thus suggesting that the enhancing effect of the convection upon the vertical circulation in MH is more than offset by the retarding influence of the higher viscosity.

A second aspect of the difference fields in Fig. 9 is the pattern of vector differences apparent at 48 h. The anticyclonic difference circulations in the west-central portion of the domain in both viscous cases, $\langle MH\rangle - \langle ML\rangle$ and $\langle DH\rangle - \langle ML\rangle$, seems

to be a geostrophic response to the pressure difference maximum shown (although the vortex center is displaced to the east). Also, the two dry cases, and particularly $\langle DL \rangle - \langle ML \rangle$, show the meso-$\alpha$ effect of the convection in ML on the horizontal winds in deflecting the westerly winds in this region to the north.

The meso-α difference fields for 9500 m are generally quite weak with the temperature and pressure anomalies weaker than those shown for 5500 m and with no coherent structure at 24 h. The vector differences are also very weak at this time. As the convective zone penetrates to this level at 48 h, however, these vector differences become quite large in this region, even with the meso-α averaging. As the undifferenced fields for $\langle ML \rangle$ in Fig. 10 show, the unsmoothed cloud zone (as in Fig. 6) occurs along the eastern boundary at 48 h. The two dry-case difference fields indicate the strong outflow on the western edge of this convective zone which causes the flow in $\langle ML \rangle$ to be deflected toward the northwest. This deflection extends to the next averaged grid point to the west in $\langle DL \rangle - \langle ML \rangle$, with downward motion in this region (in the full solution ML), indicating subsidence in the clear air upwind of the cloud. Note that the vector differences in the cloud region at this level are much larger than those occurring at 5500 m in the vicinity of the cloud (Fig. 9). It is thus apparent for this solution that the "barrier" effect of the convective zone on the meso-α scale is much more effective at the level of outflow than it is at the mid-levels, where deflection effects were shown to be present but much weaker.

Also, there seems to be an indication of increased negative pressure anomaly in the region north of the cloud in ML, implying an increase in pressure on the order of 0.5–1.0 mb in $\langle ML \rangle$ north of the convective zone. This pressure anomaly is shown in all three difference cases in Fig. 10 to be consistent geostrophically with the weak cyclonic difference circulation which occurs north of the convective zone and which implies a northward deflection of the wind in $\langle ML \rangle$.

Finally, the anticyclonic difference circulation which occurs along the southern boundary south of the cloud zone of ML in both viscous cases seems to be an effect which depends on changes in diffusivity rather than the presence or absence of the convection itself. This conclusion follows from the fact that the difference vector pattern appears to be almost identical for both viscous cases but is absent in $\langle DL \rangle - \langle ML \rangle$.

5. Meso-β features

In the previous section, we used a smoothing operator to create fields in which the smallest scale features of the solutions were eliminated and the effect of moisture and viscosity on the meso-α structure of the solutions could be displayed. In the present section, we will describe surface features with different moisture and viscosity conditions in the unsmoothed solutions in order to indicate how these parameters affect the smallest scales of the solution which we will refer to as "meso-β" features. A more detailed discussion of this meso-β structure will be given by Orlanski and Ross (1982). Here we will confine our presentation to an intercomparison of solutions so as to complete the discussion of the influence of moisture and viscosity.

Because the most intense frontal circulation occurs close to the surface, the present comparison will be done for surface conditions alone; also we will only consider solutions at 36 h, when convection is developing in the moist solutions. The meso-β disturbances are weakened considerably by the higher viscosity in cases MH and DH; therefore, only MH will be shown along with the two low-viscosity cases, ML and DL. Surface fields of the horizontal wind $\mathbf{V}$ and vertical vorticity ζ will be used to indicate the structure of the momentum field. Meso-β temperature features will be displayed in the field $\theta - \langle\theta\rangle$, which shows differences between potential temperatures in the actual solution and in the meso-α averaged solution which was described in the previous section. Such a difference field permits one to separate the meso-β anomalies from the background temperature structure.

Fig. 11 shows surface fields of $\mathbf{V}$, ζ, and $\theta - \langle\theta\rangle$ for the low-viscosity dry case DL at 36 h. A straight dashed line is drawn at the same position in each frame so as to provide a reference line which roughly corresponds to the axis of maximum vorticity along the front. The wind vector field shows that this axis approximately coincides with the axis of dilatation. Anticyclonic centers are evident in the vector field in the northwest and southeast with the front serving as a boundary between these two regions. This latter point will be discussed further by Orlanski and Ross (1982).

Reference to the plot of surface vorticity indicates that ζ is quite two-dimensional in the vicinity of the maximum value of 1.1×10^{-4} s^{-1}. On the other hand, the vector field itself indicates considerable variation in the winds along the front, particularly away from this vorticity maximum.

The potential temperature difference patterns appear to reflect the net effect of vertical motion through the upward and downward displacement of isentropes within the front. It is important to note that the smoothing operator used to generate the meso-α averaged field tends to reduce the packing of isentropes which occurs in the unsmoothed solution. Hence the temperature anomaly produced in the original solution due to vertical circulation will appear as a positive anomaly in regions of upward

motion and as a negative anomaly where the net motion is downward.

There is clearly a phase shift between the positive temperature anomaly and the axis of maximum vorticity (which is approximated by the heavy dashed line in DL). Similarly the line of maximum surface convergence is shown to also be ahead of this vorticity line at this time. As a consequence, vortex stretching, which intensified the vertical vorticity during the earlier frontogenetic stage in the life cycle of the front, now is relatively inactive. This effect has important implications for the state of equilibrium which a frontal system may achieve when full non-geostrophic effects are included. Orlanski and Ross (1982) discuss these non-geostrophic effects more thoroughly.

The inclusion of moisture in the present case can be expected to have a major effect upon the meso-β scales due to the deep convection which develops by 36 h. The surface-wind vector field in the low-viscosity, moist case ML in Fig. 12 indicates the strong convergence which is produced beneath this convective zone along a line ahead of the maximum vorticity line. The maximum intensity of the surface vorticity increases by 70% to 1.9×10^{-4} s^{-1} at this time compared to the maximum in the dry case, DL. Similarly the maximum potential temperature anomaly is more than double its value in DL. More importantly, both the temperature difference and vorticity patterns show cells developing along the front as a manifestation of the cellular structure of the upward motion in the convection above the surface front.

The primary effect of moisture is to enhance the vertical frontal circulation as free convection develops. This convection then determines the small-scale horizontal structure which is evident in $\theta - \langle\theta\rangle$ and ζ in Fig. 12. In both the dry and moist cases with low viscosity, the convergence zone is ahead of and out of phase with the vorticity zone in the frontal region at 36 h. The separation of the axes of these zones is half the width of the vorticity band, or ~100 km, at this time.

The effect of large viscosity upon meso-β features of the moist solution is shown by the case MH in Fig. 13. As expected, high wave-number features are smoothed considerably by the increase of background viscosity from 5 to 20 m^2 s^{-1}. In particular, the maximum frontal vorticity in this moist case has been reduced to 1.3×10^{-4} s^{-1}, a value close to the maximum in the dry case, DL. Also, the structure of ζ and $\theta - \langle\theta\rangle$ is similar to that of DL with no cellular structure evident at this level. Cells occur in this moist case at higher levels within the convective zone. These mid-level cells, which exhibit a somewhat larger scale than those occurring in ML, are apparently suppressed at low levels due to the increased viscosity. Finally, the plot of horizontal wind vectors shows a similar although weaker convergence zone compared to that of ML. This zone occurs on the warm air side of the axis of maximum vorticity in close correspondence to its position in the two low-viscosity cases.

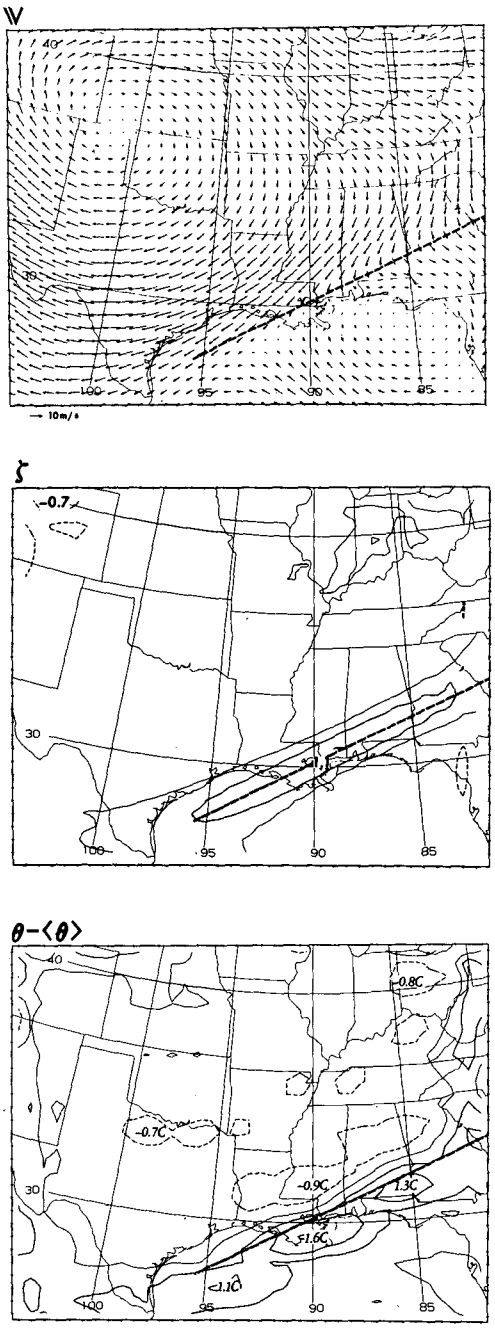

FIG. 11. Composite of fine-grid fields of case DL showing vectors (upper frame), vertical vorticity (middle frame, in units of 10^{-4} s^{-1}), and differences between unsmoothed and smoothed fields of potential temperature (bottom frame, in units of °C). A straight dashed line is included in each frame as a reference to indicate the approximate location of the axis of maximum vorticity.

6. Summary

A three-dimensional numerical model has been developed as a research tool to investigate mesoscale phenomena over a range of scales. The model uses anelastic equations of motion in order to facilitate the solution of both hydrostatic and non-hydrostatic problems. One-way nesting techniques are used to achieve higher resolution in regions of interesting mesoscale activity. Open boundary conditions are prescribed for the sides of the model with each boundary variable determined according to whether the local flow is into or out of the domain. Moist convection is treated explicitly by the model, per-

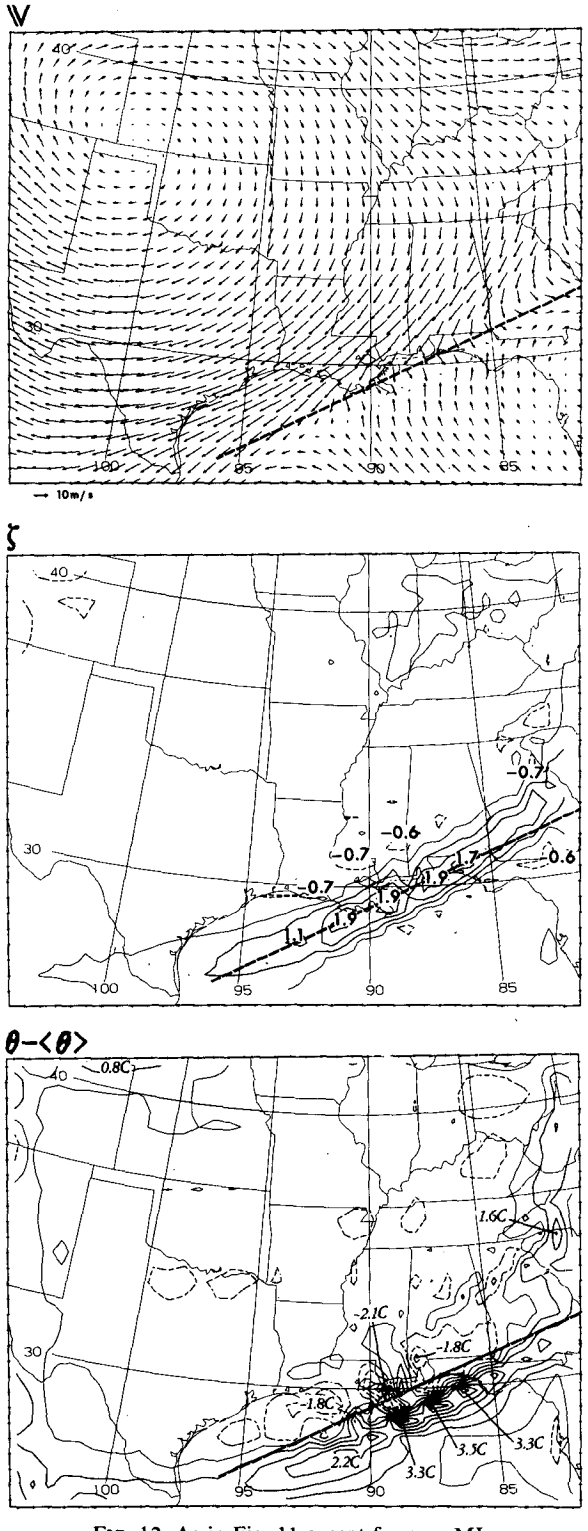

FIG. 12. As in Fig. 11 except for case ML.

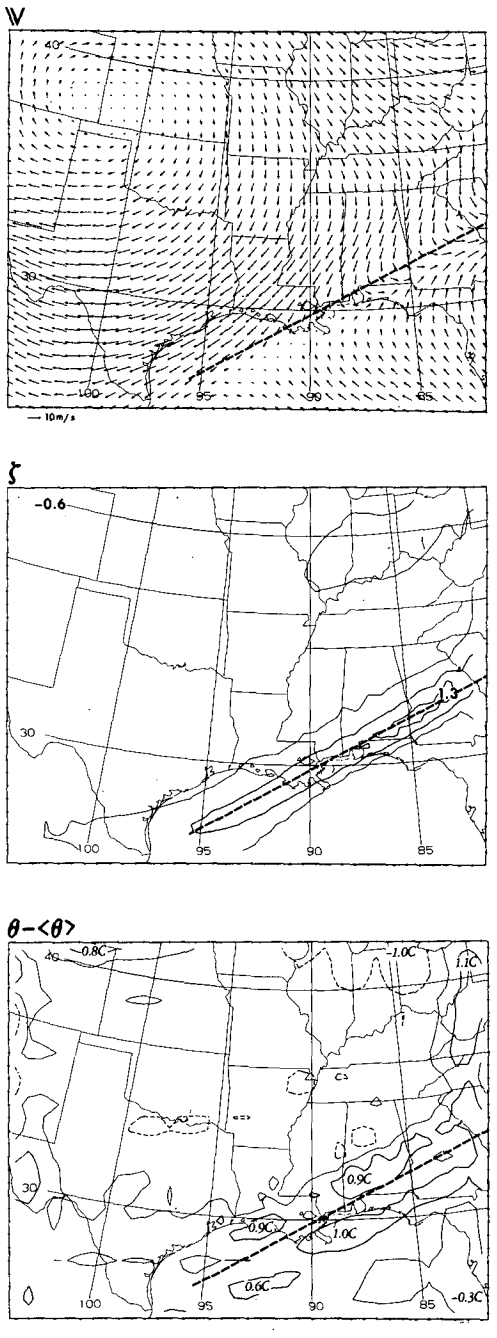

FIG. 13. As in Fig. 11 except for case MH.

mitting direct interaction between convective processes and larger-scale dynamics.

The mesoscale model is used to simulate the 48 h evolution of an observed cold front moving across the southeastern United States in a typical springtime synoptic situation. The observed system propagates as a mature front which intensifies somewhat during the early stages of the period and then weakens during the last 12 h. Moist convection occurs intermittently within the region throughout this time, mainly in the form of prefrontal squall lines.

The numerical simulation of the front's movement and intensity exhibits behavior similar to the observed evolution after an early period in which the front intensifies from its initial smooth representation on a coarse 246 km grid as prescribed from NMC data. Moist convection develops along the front after the first 24 h and then persists as an ensemble of convective cells above and somewhat ahead of the surface front for the last 24 h.

Four different simulations of the observed synoptic case have been run in order to compare the sensitivity of the frontal solution to the presence of moisture in the simulation as well as to the magnitude of the eddy viscosity used to parameterize subgrid-scale turbulence. The effects of these parameters on subsynoptic and mesoscale features of the solutions are treated separately through use of a smoothing operator which filters out scales < 250 km.

A study of the subsynoptic (or meso-α) features indicates that the largest influences of moisture and viscosity are confined to the lower levels of the atmosphere within the vicinity of the surface front. An increase in the background eddy viscosity from 5 to 20 $m^2 s^{-1}$ is shown to retard the southeastward propagation of the front by some 100 km over the first 24 h of the solution. During this early period prior to the development of active convection, the primary effect of moisture is to reduce the hydrostatic pressure in the moist region ahead of the front; this produces a change in the pressure contrast across the front of nearly 2 mb, thereby causing an increase in the surface winds along the front by as much as 3 $m s^{-1}$ through geostrophic effects.

During the last 24 h of the solution, the low-level convergence and latent heat release associated with moist convection along the front are the dominant subsynoptic features. Enhanced upward motion near the surface produces adiabatic cooling beneath the convective zone. At the same time, the diabatic heating within the cloud region creates a lower surface pressure which appears as a meso-low in the fields of pressure difference between moist and dry solutions.

The effects of moisture and viscosity on the middle and upper troposphere are weaker and more indirect than those near the surface. In particular, the region between the surface front and the jet stream is influenced by the cross-stream frontal circulation. As one might expect, this circulation is most intense in the moist, low-viscosity case and weakest when the solution contains a high viscosity and lacks moisture and the associated moist frontal convection. These differences lead to increased downward motion beneath the jet stream in the moist, low-viscosity case, thereby producing increased adiabatic warming in this region.

In addition, the deep convection occurring above the surface front penetrates to the tropopause in the later stages of the solution. The barrier effect of this cloud zone on the subsynoptic wind field seems to be largest at the level of strong convectively-driven divergence near the tropopause with only weak deflection of the wind occurring at mid-tropospheric levels.

The smaller mesoscale effects in the solutions reflect the influence of moist convection on the frontal region with viscosity differences only acting to modify this influence. Convection intensifies the vertical circulation in the front and produces a substantial increase in convergence and vertical vorticity beneath the front. The temperature and vorticity patterns in the low-viscosity solution indicate that the upward motion within the convective region has a cellular structure. Higher background viscosity, however, seems to suppress these cells, particularly near the surface.

A comparison of temperature anomalies (which are correlated with convergence as was discussed in Section 3) and vorticity at the surface within the frontal region shows a phase shift between vorticity and divergence within the mature front. The advance of the line of maximum surface convergence ahead of the corresponding vorticity line appears to be quite insensitive to viscosity differences. Orlanski and Ross (1982) will deal in more detail with the implications of this phase shift for the growth and decay of fronts and will also present an analysis of the structure and dynamics of the frontal convective system simulated by the model.

In conclusion, an investigation has been carried out on the sensitivity to viscosity and moisture effects of the mesoscale and subsynoptic scale features of a cold front system. This study suggests that the mesoscale numerical prediction of frontal characteristics such as intensity and position is feasible for time periods of up to 2 days. A major conclusion from the comparisons presented here is that the cross-stream circulation must be well resolved by the predictive model if the numerical simulation of a frontal system is to be accurate. This conclusion follows from the dynamical importance of the frontal circulation in determining many features of the front, such as position, intensity, and rainband development. In particular, the inclusion of moisture and the explicit treatment of convection have been shown to

improve the mesoscale structure of the front by intensifying this circulation. Thus, it would appear from our results that numerical models will need to resolve meso-β scales if they are to predict the detailed behavior of frontal systems in a realistic manner for periods up to 48 h.

Acknowledgments. The authors are most grateful to Messrs. Rich Shaginaw and Larry Polinsky for their programming assistance, to Mr. Shaginaw and Dr. Frank Lipps for their help in making the manuscript more readable, and to one of the reviewers, Dr. Kerry Emanuel, for his thorough review. We also would like to thank Dr. Ian Simmonds for providing the spline interpolation subroutine and the NCAR computing staff for providing the graphical map data of North America which are used in the figures. Finally, we appreciate the patience and skill exhibited by Mrs. Betty Williams in typing the manuscript and by Messrs. John Connor, Phil Tunison, Mike Zadworney and Bill Ellis in preparing the figures.

APPENDIX A

Details of Open Boundary Conditions

a. *Evaluation of inflow/outflow conditions*

A normalized phase velocity δ, which is proportional to the mean of the local observed and model velocity components normal to the boundary, is used to determine whether a given boundary point is inflow or outflow for purposes of the open boundary algorithm. For example, δ is computed as follows for the position $y = (J - 1)\Delta y$ along the western boundary:[11]

$$\delta_J = -\frac{\Delta t}{\Delta x}\frac{u_{2J}^{\tau} + u_{\text{obs}J}^{\tau}}{2}, \tag{A.1}$$

where the quantity u_{2J}^{τ} refers to the boundary wind component u in the model solution at time $\tau\Delta t$ and position $x = (2 - 1)\Delta x$, $y = (J - 1)\Delta y$. The quantity $u_{\text{obs}J}^{\tau}$ is the observed (or coarse-model) value of u at position $y = (J - 1)\Delta y$ along the west boundary. Note that, in the case of a nested model, this phase speed δ_J can be viewed as representing a spatial average between the normal velocity located just inside the fine model domain and the normal velocity located in the coarser model domain just outside of the boundary interface.

The inflow/outflow decision is then made for the western boundary point J according to whether $\delta_J \leq 0$ (inflow) or $\delta_J > 0$ (outflow).

[11] For the sake of clarity of presentation, the vertical index K will be dropped from all finite difference variables in this appendix unless stated otherwise. Each expression presented here is assumed to apply to the vertical level $z = (K - \frac{1}{2})\Delta z$.

1) TREATMENT OF VELOCITY FIELD

As described in Section 2d, the vertical vorticity ζ and the horizontal divergence D are used together to determine the boundary values for u and v. For the sake of exposition, we will continue with the discussion of treatment of the western boundary point located at array location $(1, J)$. The reader is directed to Fig. 14 for a display of the horizontal grid spacing along the western boundary where boundary points for u and v are circled while boundary points for D and ζ are enclosed in boxes.

The following two possibilities exist for the calculation of vertical vorticity $\zeta_{2J}^{\tau+1}$ at the west boundary:

1) For outflow points where $\delta_J > 0$, vorticity is "advected" using one-sided differencing as

$$\zeta_{2J}^{\tau+1} = \zeta_{2J}^{\tau} - \delta_J(\zeta_{2J}^{\tau} - \zeta_{3J}^{\tau}). \tag{A.2}$$

2) For inflow points where $\delta_J \leq 0$, we use the observed vorticity

$$\zeta_{2J}^{\tau+1} = \zeta_{\text{obs}J}^{\tau+1}. \tag{A.3}$$

The vorticity determined by either (A.2) or (A.3) at each point is then separated into a barotropic part $\overline{\rho_0\zeta_{2J}}^{\tau+1}$ and a baroclinic part $(\rho_0\zeta_{2J}^{\tau+1})'$. The baroclinic part is used directly to obtain the boundary condition for the baroclinic tangential velocity component from the definition of vorticity. Thus for the western boundary example:

$$(\rho_0 v_{2J}^{\tau+1})' = (\rho_0 v_{3J}^{\tau+1})' - \frac{\Delta x}{\Delta y}[(\rho_0 u_{2J+1}^{\tau})' - (\rho_0 u_{2J}^{\tau})'] - \Delta x(\rho_0\zeta_{2J}^{\tau+1})', \tag{A.4}$$

where the interior value $(\rho_0 v_{3J}^{\tau+1})'$ was obtained from the baroclinic prognostic equation (2.14). The lagging in time of the y-derivative of variable $\rho_0 u$ in this expression was found empirically to be necessary in order to maintain both the stability of the scheme and its explicit computational character.

The barotropic part $\overline{\rho_0\zeta_{2J}}^{\tau+1}$ is used as part of the forcing function for the Poisson equation (2.21) at the points adjacent to the boundaries (In fact, this may be viewed as a condition which partially determines the barotropic velocity component tangential to the model boundaries.).

In calculating the interim value $D_{2J}^{*\tau+1}$ for the horizontal divergence at the boundary, we identify two possible conditions:

1) For outflow points ($\delta_J > 0$), a simple radiation condition is used, *viz*:

$$D_{2J}^{*\tau+1} = D_{3J}^{\tau}, \tag{A.5}$$

which implies a outward phase speed $\Delta x/\Delta t$.

2) For inflow points ($\delta_J \leq 0$), the baroclinic ob-

served normal velocity at the boundary is used along with adjacent baroclinic velocity components from the interior solution to compute an "observed" divergence as:

$$D_{2J}^{*\tau+1} = -\frac{1}{\Delta x}[(\rho_0 u_{2J}{}^{\tau+1})' - (\rho_0 u_{\text{obs}J}{}^{\tau+1})'] - \frac{1}{\Delta y}[(\rho_0 v_{2J}{}^{\tau})' - (\rho_0 v_{2J-1}{}^{\tau})'], \quad \text{(A.6)}$$

where the time-advanced quantity $(\rho_0 u_{2J}{}^{\tau+1})'$ is obtained from the prognostic equation (2.14). Also as in (A.4), the lagging of the y-momentum $\rho_0 v$ to time $\tau\Delta t$ was found to be needed to maintain stability.

The resulting divergence over the vertical column at boundary point J now consists of the interim divergence D^* as determined at each vertical level K from (A.5) or (A.6). The divergence in this column must then be made baroclinic so that

$$\frac{1}{H}\sum_{K=2}^{J-1} D_{2JK}\Delta z = \rho_0 w_{\text{top}} - \rho_0 w_{\text{surface}} = 0,$$

where K is shown explicitly here. Hence we require that the final boundary divergence be

$$D_{2J}^{\tau+1} = (D_{2J}^{*\tau+1})'. \quad \text{(A.7)}$$

Finally, this divergence is used to obtain the baroclinic normal velocity around the boundary using the finite-difference expression for divergence. For the western boundary example, the normal velocity component

$$(\rho_0 u_{1J}{}^{\tau+1})' = (\rho_0 u_{2J}{}^{\tau+1})' + \frac{\Delta x}{\Delta y}[(\rho_0 v_{2J}{}^{\tau})' - (\rho_0 v_{2J-1}{}^{\tau})'] - \Delta x D_{2J}{}^{\tau+1}. \quad \text{(A.8)}$$

Eqs. (A.4) and (A.8) thus provide boundary conditions for the baroclinic velocity components. These components, together with their first interior rows, are then smoothed using a smoothing procedure (described in subsection *b* below) in order to eliminate large horizontal gradients which may develop at transition zones of inflow/outflow along the boundary.

The vertical momentum component $\rho_0 w^{\tau+1}$ is determined at the boundary using outward extrapolation with maximum propagation speed $\Delta x/\Delta t$. Thus for the western boundary example, we have the condition

$$\rho_0 w_{2J}{}^{\tau+1} = \rho_0 w_{3J}{}^{\tau}. \quad \text{(A.9)}$$

This boundary condition is employed instead of a direct computation from the boundary divergence because the latter method has been shown to produce excessively large values of $\rho_0 w^{\tau+1}$ at inflow points when a large difference develops between the observed and interior normal velocity. Condition (A.9) is intended to simulate the rapid propagation of gravity waves out of the domain and is consistent with the divergence condition (A.5) above when the entire boundary column is outflow.

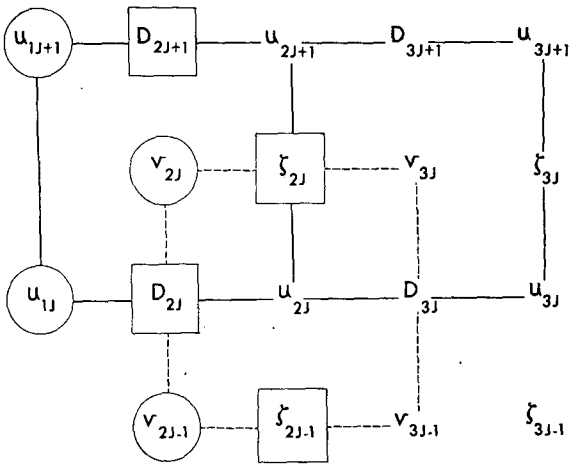

FIG. 14. Horizontal grid configuration along the western boundary for velocity components u and v, horizontal divergence D, and vertical vorticity ζ. Boundary velocity points are circled, while boundary divergence and vorticity points are enclosed in boxes. The subscript notation is defined in the text.

2) TREATMENT OF THE THERMODYNAMIC VARIABLES

The boundary procedure for the thermodynamic variables θ, q, and c uses a radiative condition for outflow and a prescribed observed value for inflow. As before, inflow/outflow conditions are determined by the phase speed δ_J directed normal to the boundary as in (A.1). When boundary conditions indicate outflow, however, tangential as well as normal advection is used in the radiation condition since the model solutions have been shown to be very sensitive locally to the structure of θ at the boundary.

The boundary procedure for any of the three variables θ, q, or c at the boundary point (2, J) is given below for the case of potential temperature θ on the western boundary:

1) For inflow points ($\delta_J \leq 0$), use the observed potential temperature as

$$\theta_{2J}{}^{\tau+1} = \theta_{\text{obs}J}{}^{\tau+1}. \quad \text{(A.10)}$$

2) For outflow points ($\delta_J > 0$), assume a radiation condition with upwind differencing in the normal and tangential directions using the normalized tangential phase speed

$$\delta_J' = \frac{\Delta t}{\Delta x}\frac{v_{2J}{}^{\tau} + v_{2J-1}{}^{\tau}}{2}. \quad \text{(A.11)}$$

Then two possible boundary expressions are used, depending upon the sign of $\delta_J{}'$:

$$\theta_{2J}{}^{\tau+1} = \theta_{2J}{}^{\tau} - \delta_J(\theta_{2J}{}^{\tau} - \theta_{3J}{}^{\tau}) - \delta_J{}'(\theta_{2J}{}^{\tau} - \theta_{2J-1}{}^{\tau})$$

if

$$\delta_J{}' > 0 \qquad \text{(A.12a)}$$

or

$$\theta_{2J}{}^{\tau+1} = \theta_{2J}{}^{\tau} - \delta_J(\theta_{2J}{}^{\tau} - \theta_{3J}{}^{\tau}) + \delta_J{}'(\theta_{2J}{}^{\tau} - \theta_{2J+1}{}^{\tau})$$

if

$$\delta_J{}' \leqslant 0. \qquad \text{(A.12b)}$$

The resulting potential temperatures on the boundary are then smoothed using the procedure described in the following subsection. No smoothing is done when the above procedure is applied to q or c.

b. Boundary smoothing

In order to minimize the singular behavior at the boundary where inflow changes to outflow or vice versa (and the phase velocity relevant to the boundary procedure is tangential to the boundary), we perform a horizontal smoothing of the boundary data around the limited area domain. This smoothing consists of the low-pass filter proposed by Shapiro (1970), which consists of the following four-step operator which only differs in the value of the coefficient S_n:

$$\theta_{2J}{}^{(n+1)} = \theta_{2J}{}^{(n)} + S_n(\theta_{2J-1}{}^{(n)} + \theta_{2J+1}{}^{(n)} - 2\theta_{2J}{}^{(n)}),$$

$$n = 1, 2, 3, 4, \qquad \text{(A.13)}$$

where

$$S_1 = \tfrac{1}{4},\ S_2 = -\tfrac{1}{4},\ S_3 = \tfrac{1}{4}\sqrt{-1},\ S_4 = -\tfrac{1}{4}\sqrt{-1}.$$

The initial $\theta_{2J}{}^{(1)}$ is the value of potential temperature (here on the western boundary) at the beginning of each smoothing iteration.

This four-step operation is applied iteratively each time step to the boundary fields of u, v, and θ, with the number of iterations varying according to the desired amount of damping of the high wave numbers, to the type of variable, and to the model resolution involved. In the present case, 100 iterations are used for u and v in the 61.5 km grid solutions while only three are used in the 246 km grid case. In both cases, potential temperature is smoothed with three iterations. Note also that the horizontal row of variables to be smoothed is periodic since it forms a closed line of points extending around the circumference of the domain. As a result, even higher-order smoothing operators (Shapiro, 1970) may be easily applied to the boundary data to be even more selective in damping only $2\Delta x$ waves.

APPENDIX B

Summary of Initialization Procedures

In this appendix we will present a description of the steps involved in the initialization procedures summarized in Section 2e. The subscripts 1, 2, and 3 will be used here to denote respectively: 1) observed data on the N40 grid on constant pressure surfaces, 2) coarse mesoscale data on the meso-α (246-km) grid, and 3) finer mesoscale data on the meso-β (61.5 km) grid. Square brackets will be used around a variable to designate that the variable has been interpolated to the finer grid indicated by the subscript on the brackets. For example, the quantity "$[\zeta_1]_2$" refers to the vorticity data which is defined on the mesogrid after having been interpolated from the vorticity ζ_1 on the N40 grid.

The step-by-step procedures which were used for the coarse model initialization are as follows:

1) Compute vorticity ζ_1 from streamfunction ψ_1 in the observed data. Convert temperature T_1 to potential temperature θ_1.

2) Interpolate variables ψ_1, ζ_1, θ_1, R_1 and ϕ_1 in constant pressure surfaces from the N40 to the coarse mesoscale grid using the 12-point interpolation scheme developed by Shapiro (1972).

3) Use cubic splines (Ahlberg *et al.*, 1967) to vertically interpolate all variables from constant-pressure to constant-height levels using geopotential height $[\phi_1]_2$.

4) Reconstruct the interim streamfunction ψ_2^* in constant-height surfaces from the interpolated vorticity $[\zeta_1]_2$ by solving a Poisson equation with streamfunction boundary conditions derived from the interpolated velocity components $[u_1]_2$ and $[v_1]_2$. The domain of interest for the mesoscale model will consist of a smaller interior region from this full field.

5) Maintain the observed barotropic pressure but modify the baroclinic pressure such that it is consistent in its hydrostatic dependence upon the interpolated potential temperature $[\theta_1]_2$.

6) Compute the barotropic geostrophic streamfunction $\bar{\psi}_{g2}$ from the observed barotropic pressure $\overline{\pi_2}$ by solving the Poisson equation $\nabla^2\bar{\psi}_{g2} = -c_p\theta_0\nabla^2(\overline{\pi_2}/f)$. Replace the observed barotropic value $\bar{\psi}_2^*$ with this value in the streamfunction field ψ_2^* to obtain the final streamfunction ψ_2. Compute the horizontal wind components u_2 and v_2 from ψ_2.

The final model variables are then u_2, v_2, $[\theta_1]_2$, $[R_1]_2$, and π_2 with the relative humidity $[R_1]_2$ converted to water vapor mixing ratio q_2 in the model. The vertical velocity w_2 is zero since the initial conditions are non-divergent. Cloud water mixing ratio c_2 is also zero.

The step-by-step procedure for nested-data initialization is performed as follows:

1) Compute higher-order quantities ζ_2, $\nabla \cdot \mathbf{V}_2$, and $\nabla^2\theta_2$ on the coarse grid.

2) Incorporate observed relative humidity $[R_1]_2$ into the coarse data set, if necessary.

3) Interpolate all variables in the horizontal using the 12-point Shapiro interpolation procedure.

4) If necessary, interpolate in the vertical using splines.

5) In order to reconstruct the horizontal wind at each z level on the fine grid, the streamfunction ψ_3 on the domain boundaries is first determined by integrating the velocity components normal to the domain boundary around the domain. Because the field is divergent, a constant normal velocity is subtracted from each boundary velocity so that this boundary streamfunction can be obtained. The Poisson equation

$$\nabla^2\psi_3 = -[\zeta_2]_3 , \tag{B1}$$

is then solved using the boundary streamfunction obtained above.

In order to obtain the divergent field, one then determines the normal derivative for the velocity potential Φ_3, namely:

$$\frac{\partial\Phi_3}{\partial n} = [\mathbf{V}_2]_3 \cdot \mathbf{n} + \frac{\partial\psi_3}{\partial s}, \tag{B2}$$

where the unit vector $\mathbf{n}$ is directed into the domain and the tangential coordinate s increases in a counterclockwise direction about the domain. The velocity $[\mathbf{V}_2]_3 = [u_2]_3\mathbf{i} + [v_2]_3\mathbf{i}$ is the wind field interpolated to the fine grid. The Poisson equation

$$\nabla^2\Phi_3 = [\nabla \cdot \mathbf{V}_2]_3 , \tag{B3}$$

is then solved using the above Neumann condition (B2). Finally the new velocity components are constructed as

$$\left.\begin{aligned} u_3 &= \frac{\partial\Phi_3}{\partial x} + \frac{\partial\psi_3}{\partial y} \\ v_3 &= \frac{\partial\Phi_3}{\partial y} - \frac{\partial\psi_3}{\partial x} \end{aligned}\right\} . \tag{B4}$$

6) The potential temperature θ_3 is reconstructed by solving the Poisson equation

$$\nabla^2\theta_3 = [\nabla^2\theta_2]_3 , \tag{B5}$$

using interpolated boundary data $[\theta_2]_3$.

REFERENCES

Ahlberg, J. H., E. N. Nilson and J. L. Walsh, 1967: *The Theory of Splines and their Applications*, Academic Press, 284 p.

Blumen, W., 1980: A comparison between the Hoskins-Bretherton model of frontogenesis and the analysis of an intense surface frontal zone. *J. Atmos. Sci.*, **37**, 64–77.

Hobbs, P. V., and K. R. Biswas, 1979: The cellular structure of narrow cold-frontal rainbands. *Quart. J. Roy. Meteor. Soc.*, **105**, 723–727.

Hoskins, B. J., 1971: Atmospheric frontogenesis models: Some solutions. *Quart. J. Roy. Meteor. Soc.*, **97**, 139–153.

——, and N. V. West, 1979: Baroclinic waves and frontogenesis. Part II: Uniform potential vorticity jet flows—cold and warm fronts. *J. Atmos. Sci.*, **36**, 1663–1680.

James, P. K., and K. A. Browning, 1979: Mesoscale structure of line convection at surface cold fronts. *Quart. J. Roy. Meteor. Soc.*, **105**, 371–382.

McWilliams, J. C., and P. R. Gent, 1980: Intermediate models of planetary circulations in the atmosphere and ocean. *J. Atmos. Sci.*, **37**, 1657–1678.

Meisinger, F., and A. Arakawa, 1976: Numerical methods used in atmospheric models, Vol. 1. GARP Publ. Ser. No. 17, WMO, 64 pp.

Miyakoda, K., 1973: Cumulative results of testing a meteorological-mathematical model: the description of the model. *Proc. Roy. Irish Acad.*, **A73**, 99–130.

Ogura, Y., and M-T. Liou, 1980: The structure of a mid-latitude squall line: A case study. *J. Atmos. Sci.*, **37**, 553–567.

——, and N. A. Phillips, 1962: Scale analysis of deep and shallow convection in the atmosphere. *J. Atmos. Sci.*, **19**, 173–179.

Orlanski, I., 1976: A simple boundary condition for unbounded hyperbolic flows. *J. Comput. Phys.*, **21**, 251–269.

——, and B. B. Ross, 1977: The circulation associated with a cold front. Part I: Dry case. *J. Atmos. Sci.*, **34**, 1619–1633.

——, and ——, 1982: The evolution of an observed cold front. Part II: Mesoscale dynamics. To be submitted to *J. Atmos. Sci.*

——, —— and L. J. Polinsky, 1974: Diurnal variation of the planetary boundary layer in a mesoscale model. *J. Atmos. Sci.*, **31**, 965–989.

Robert, A. J., 1966: The integration of a low-order spectral form of the primitive meteorological equations. *J. Meteor. Soc. Japan*, **44**, 237–245.

Ross, B. B., and I. Orlanski, 1978: The circulation associated with a cold front. Part II: Moist case. *J. Atmos. Sci.*, **35**, 445–465.

Shapiro, R., 1970: Smoothing, filtering, and boundary effects. *Rev. Geophys. Space Phys.*, **8**, 359–387.

Shapiro, R., 1972: Information loss and compensation in linear interpolation. *J. Comput. Phys.*, **10**, 65–84.

Smagorinsky, J., 1960: On the dynamical prediction of large-scale condensation by numerical methods. *Geophys. Monogr.*, No. 5, Amer. Geophys. Union, 71–78.

Williams, G. P., 1969: Numerical integration of the three-dimensional Navier-Stokes equations for incompressible flow. *J. Fluid. Mech.*, **37**, 727–750.

Williams, R. T., 1967: Atmospheric frontogenesis: A numerical experiment. *J. Atmos. Sci.*, **24**, 627–641.

Zipser, E. J., 1977: Mesoscale and convective-scale downdrafts as distinct components of squall-line structure. *Mon. Wea. Rev.*, **105**, 1568–1589.